

A VLA STUDY OF HIGH-REDSHIFT GRBS II – THE COMPLEX RADIO AFTERGLOW OF GRB 140304A: SHELL COLLISIONS AND TWO REVERSE SHOCKS

TANMOY LASKAR^{1,2}, EDO BERGER³, RAFFAELLA MARGUTTI⁴, ASHLEY ZAUDERER⁵, PETER K. G. WILLIAMS³,
 WEN-FAI FONG^{6,7}, RE'EM SARI⁸, KATE D. ALEXANDER³, AND ATISH KAMBLE³

Draft version July 18, 2017

ABSTRACT

We present detailed multi-frequency, multi-epoch radio observations of GRB 140304A at $z = 5.283$ from 1 to 86 GHz and 0.45 d to 89 d. The radio and mm data exhibit unusual multiple spectral components, which cannot be simply explained by standard forward and reverse shock scenarios. Through detailed multi-wavelength analysis spanning radio to X-rays, we constrain the forward shock parameters to $E_{K,iso} \approx 4.9 \times 10^{54}$ erg, $A_* \approx 2.6 \times 10^{-2}$, $\epsilon_e \approx 2.5 \times 10^{-2}$, $\epsilon_B \approx 5.9 \times 10^{-2}$, $p \approx 2.6$, and $\theta_{jet} \approx 1.1^\circ$, yielding a beaming corrected γ -ray and kinetic energy, $E_\gamma \approx 2.3 \times 10^{49}$ erg and $E_K \approx 9.5 \times 10^{50}$ erg, respectively. We model the excess radio emission as due to a combination of a late-time reverse shock (RS) launched by a shell collision, which also produces a re-brightening in the X-rays at ≈ 0.26 d, and either a standard RS or diffractive interstellar scintillation. Under the standard RS interpretation, we invoke consistency arguments between the forward and reverse shocks to derive a deceleration time, $t_{dec} \approx 100$ s, the ejecta Lorentz factor, $\Gamma(t_{dec}) \approx 300$, and a low RS magnetization, $R_B \approx 0.6$. Our observations highlight both the power of radio observations in capturing RS emission and thus constraining the properties of GRB ejecta and central engines, and the challenge presented by interstellar scintillation in conclusively identifying RS emission in GRB radio afterglows.

1. INTRODUCTION

The mechanism producing the relativistic jets responsible for long-duration γ -ray bursts (GRBs) is understood to involve a compact central engine such as a magnetar or accreting black hole, formed during core collapse of a massive star (Woosley & Bloom 2006; Piran 2005; Metzger et al. 2011). A crucial clue to uncovering the nature of this mechanism and of the engine is provided by studies of GRB jets, requiring detailed observations and theoretical modeling of both the prompt γ -ray radiation from magnetic reconnection or shell collisions within the jet itself, and the afterglow generated when the jet is decelerated by the circumburst environment (Sari et al. 1998).

Facilitated by data from *Swift* and *Fermi*, such studies have revealed complex spectral and temporal features in both the prompt emission and the afterglow, suggesting that GRB jets are episodic and variable; theoretical studies suggest the variability may be an intrinsic feature of the jet acceleration mechanism (Fenimore et al. 1999; Aloy et al. 2002;

Morsony et al. 2010; López-Cámara et al. 2016). While internal shocks within the ejecta arising from the collision of material moving with different Lorentz factors are believed to be responsible for the production of the prompt γ -ray radiation (Kobayashi et al. 1997; Daigne & Mochkovitch 1998), long-lasting central engine activity is a leading model for flares observed in their X-ray afterglows (Fan & Wei 2005; Falcone et al. 2006; Chincarini et al. 2007, 2010; Margutti et al. 2010a, 2011a,b; Bernardini et al. 2011).

The observed γ -ray variability and late-time X-ray and optical flaring activity has encouraged a range of theoretical models predicting ejecta stratification, including fragmentation of the accretion disk due to viscous instabilities, two-stage collapse, fallback accretion, variability in the accretion rate, and shell collisions (King et al. 2005; Perna et al. 2006; Proga & Zhang 2006; Ghisellini et al. 2009; Vlasov et al. 2011; Geng et al. 2013; Guidorzi et al. 2015; Yu et al. 2015; Dall’Osso et al. 2017). The resulting structured ejecta profiles are expected to have a long-term impact on the afterglow, producing a long-lasting energy injection phase as slower shells catch up with the forward shock (FS; Sari & Mészáros 2000). The injection is expected to flatten the afterglow decay, and, if it occurs rapidly enough, to cause an achromatic re-brightening in the afterglow light curves (Kumar & Piran 2000; Zhang & Mészáros 2002; Granot et al. 2003; Beniamini & Mochkovitch 2017). Such simultaneous optical and X-ray re-brightenings have been seen in a few instances (Mangano et al. 2007; Margutti et al. 2010b; Holland et al. 2012; Li et al. 2012; Greiner et al. 2013; Panaitescu et al. 2013; Nardini et al. 2014; De Pasquale et al. 2015).

The injection process is expected to be accompa-

¹ National Radio Astronomy Observatory, 520 Edgemont Road, Charlottesville, VA 22903, USA

² Department of Astronomy, University of California, 501 Campbell Hall, Berkeley, CA 94720-3411, USA

³ Harvard-Smithsonian Center for Astrophysics, 60 Garden St, Cambridge, MA 02138, USA

⁴ Center for Interdisciplinary Exploration and Research in Astrophysics (CIERA) and Department of Physics and Astrophysics, Northwestern University, Evanston, IL 60208, USA

⁵ Center for Cosmology and Particle Physics, New York University, 4 Washington Place, New York, NY 10003, USA

⁶ Einstein Fellow

⁷ Steward Observatory, University of Arizona, 933 N. Cherry Ave, Tucson, AZ 85721, USA

⁸ Racah Institute of Physics, The Hebrew University, Jerusalem 91904, Israel

nied by a reverse shock (RS) if the collision between shells is violent, i.e., at large relative Lorentz factor (Zhang & Mészáros 2002). Identification and characterization of this RS may lead to deeper insight into the jet production mechanisms, and by extension, the accretion process. Whereas multi-wavelength modeling of the observed X-ray to radio light curves suggests that complex ejecta profiles may be ubiquitous in GRB afterglows, these studies did not find evidence for the injection RS, possibly due to physical effects such as the shell collision process being gentle, or due to observational constraints, such as limited wavelength coverage and temporal sampling of the spectral energy distribution (SED) of the afterglow (Laskar et al. 2015). In particular, the RS produced by shell collisions is expected to peak in the mm-band, where observational facilities have been scarce (de Ugarte Postigo et al. 2012).

In Paper I of this series, we introduced our VLA study of radio afterglows of GRBs at $z \gtrsim 5$ (Laskar et al. 2017, submitted). Here, we present radio through X-ray observations of GRB 140304A at $z = 5.283$, together with detailed multi-band modeling using physical afterglow models. The radio and mm observations exhibit multiple components, which cannot be explained as a standard FS and RS combination. We interpret the data in the context of a model requiring a RS initiated by a shell collision, and show that the resultant SEDs and light curves are consistent with the signatures of energy injection visible in the X-ray and optical observations of this event. The model suggests expansion into a wind-like medium, and identification of one of the radio components as the standard RS yields a measurement of the ejecta Lorentz factor at the deceleration time. We employ a standard cosmology of $\Omega_m = 0.31$, $\Omega_\Lambda = 0.69$, and $H_0 = 68 \text{ km s}^{-1} \text{ Mpc}^{-1}$, all magnitudes are in the AB system, all uncertainties are at 1 sigma, and all times refer to the observer frame, unless otherwise specified.

2. GRB PROPERTIES AND OBSERVATIONS

GRB 140304A was discovered by the *Swift* Burst Alert Telescope (BAT, Barthelmy et al. 2005) on 2014 March 4 at 13:22:31 UT (Evans et al. 2014). The burst duration in the 15–350 keV BAT energy band is $T_{90} = 15.6 \pm 1.9 \text{ s}$, with a fluence of $F_\gamma = (1.2 \pm 0.1) \times 10^{-6} \text{ erg cm}^{-2}$ (15–150 keV; Baumgartner et al. 2014). A bright optical afterglow was detected by the MASTER robotic network (Gorbovskey et al. 2014a), subsequently confirmed by other ground-based observatories (Xu et al. 2014; Volnova et al. 2014a,b; de Ugarte Postigo et al. 2014). Spectroscopic observations 8.2 hr after the burst at the 10.4 m Gran Telescopio Canarias (GTC) provided a redshift of $z = 5.283$ (Jeong et al. 2014).

The burst also triggered the *Fermi* Gamma-ray Burst Monitor (GBM) at 13:22:31.48 UT (Jenke & Fitzpatrick 2014). The burst duration in the 50–300 keV GBM band is $T_{90} = 32 \pm 6 \text{ s}$ with a fluence of $(2.0 \pm 0.2) \times 10^{-6} \text{ erg cm}^{-2}$ (10–1000 keV). A Band-function fit to the time-averaged γ -ray spectrum⁹ yields a break energy, $E_{\text{peak}} = 123 \pm 27 \text{ keV}$, low energy index, $\alpha = -0.80 \pm 0.22$, and high-energy index, $\beta = -2.35 \pm 0.43$. Using the source redshift of $z = 5.283$, the inferred isotropic equiv-

alent γ -ray energy in the $1\text{--}10^4 \text{ keV}$ rest frame energy band is $E_{\gamma,\text{iso}} = (1.2 \pm 0.2) \times 10^{53} \text{ erg}$.

2.1. X-ray: *Swift*/XRT

The *Swift* X-ray Telescope (XRT, Burrows et al. 2005b) began observing the field at 75.2 seconds after the BAT trigger, leading to the detection of an X-ray afterglow. The source was localized to RA = 2h 2m 34.26s, Dec = +33d 28' 25.7" (J2000), with an uncertainty radius of 1.5" (90% containment)¹⁰. XRT continued observing the afterglow for 5.3 d in photon counting mode, with the last detection at 3.0 d.

We extracted XRT PC-mode spectra using the on-line tool on the *Swift* website (Evans et al. 2007, 2009)¹¹ in the intervals 125 s to 1557 s (spectrum 1) and 5192 s to $5.78 \times 10^5 \text{ s}$ (spectrum 2)¹². We downloaded the event and response files generated by the on-line tool in these time bins, and fit them using the HEASOFT (v6.16) and corresponding calibration files. We used Xspec to fit all available PC-mode data, assuming a photoelectrically absorbed power law model (`tbabs` \times `ztbabs` \times `pow`), fixing the galactic absorption column at $N_{\text{H,Gal}} = 7.68 \times 10^{20} \text{ cm}^{-2}$ (Willingale et al. 2013), and tying the value of the intrinsic absorption in the host galaxy, $N_{\text{H,int}}$, to be the same between the two spectra since we do not expect any evolution in the intrinsic absorption with time. We find marginal evidence for spectral evolution between the two spectra across the orbital gap; the results are summarized in Table 1. In the following analysis, we take the 0.3–10 keV count rate light curve from the *Swift* website and compute the 1 keV flux density using our spectral models, with $\Gamma_X = 1.87$ before 1557 s and $\Gamma_X = 2.27$ thereafter. We combine the uncertainty in flux calibration based on our spectral analysis (7% in spectrum 1 and 16% in spectrum 2) in quadrature with the statistical uncertainty from the on-line light curve.

For the WT-mode, we convert the count rate light curve to a flux-calibrated light curve using $\Gamma = 2.5$ and an unabsorbed count-to-flux conversion factor of $3.9 \times 10^{-11} \text{ erg cm}^{-2} \text{ ct}^{-1}$ as reported on the *Swift* website. The WT-mode X-ray light curve declines rapidly as $t^{-4.0 \pm 0.8}$ to $1.3 \times 10^{-3} \text{ d}$. Similar early, rapidly declining X-ray light curves are frequently observed in XRT light curves, and have been speculated to arise from the high-latitude component of the prompt emission (Kumar & Panaitescu 2000; Tagliaferri et al. 2005; Nousek et al. 2006; Willingale et al. 2010). Alternatively, this steep decay could also arise from the end of a preceding flare, the beginning of which was missed during spacecraft slew. The PC mode data beginning at 146 s are also dominated by flaring activity until $\approx 2 \times 10^{-2} \text{ d}$. We therefore do not consider the X-ray data before $2 \times 10^{-2} \text{ d}$ in our afterglow modeling.

2.2. Optical

The *Swift* UV/Optical Telescope (UVOT, Roming et al. 2005) observed GRB 140304A beginning 138 s after the burst (Marshall & Evans 2014). We

⁹ From the *Fermi* GRB catalog for trigger 140304557

¹⁰ http://www.swift.ac.uk/xrt_positions/00590206/

¹¹ http://www.swift.ac.uk/xrt_spectra/00590206/

¹² All analysis reported in this section excludes the flare between 20 ks and 23 ks

Table 1
XRT Spectral Analysis for GRB 140304A

Parameter	Spectrum 1	Spectrum 2
T_{start} (s)	125	5192
T_{end} (s)	1557	5.78×10^5
$N_{\text{H,gal}}$ (10^{20} cm^{-2})		5.98
$N_{\text{H,int}}$ (10^{22} cm^{-2})		$3.8^{+1.5}_{-1.4}$
Photon index, Γ	1.87 ± 0.07	2.27 ± 0.15
Flux (obs [†])	$1.61^{+0.11}_{-0.10} \times 10^{-10}$	$1.62^{+0.30}_{-0.23} \times 10^{-13}$
Flux (unabs [‡])	2.0×10^{-10}	2.3×10^{-13}
Counts to flux (obs [†])	2.6×10^{-10}	3.6×10^{-11}
Counts to flux (unabs [‡])	3.3×10^{-10}	5.1×10^{-11}
C statistic (dof)	425 (469)	

Note. — [†]0.3–10 keV, observed ($\text{erg cm}^{-2} \text{ s}^{-1}$); [‡]0.3–10 keV unabsorbed ($\text{erg cm}^{-2} \text{ ct}^{-1}$).

Table 2
Swift UVOT Observations of GRB 140304A

Δt (d)	Filter	3σ Flux Upper Limit ^a (mJy)
7.08×10^{-2}	<i>white</i>	2.38×10^1
7.60×10^{-2}	<i>b</i>	3.70×10^1
2.67×10^{-1}	<i>b</i>	7.24×10^1
...

Note. — This is a sample of the full table available on-line.

analyzed the UVOT data using HEASOFT (v. 6.16) and corresponding calibration files and list our derived upper limits in Table 2. We compiled all observations reported in GCN circulars and present the compilation in Table 3.

2.3. Millimeter: CARMA

We observed GRB 140304A with the Combined Array for Research in Millimeter Astronomy (CARMA) beginning on 2014 March 04.02 UT (0.54 d after the burst) in continuum wideband mode with 8 GHz bandwidth (16 windows, 487.5 MHz each) at a mean frequency of 85.5 GHz. Following an initial detection (Zauderer et al. 2014), we obtained two additional epochs. All observations utilized J0237+288 as phase calibrator. The first two epochs additionally utilized 3C84 as bandpass calibrator and Uranus as flux calibrator. For the third epoch, the array shut down due to high winds, truncating observations at a total track length of 1.9 h and preventing observations of the flux calibrator.

We derived a linelength calibration to account for thermal changes in the delays through the optical fibers connecting the CARMA antennas to the correlator using MIRIAD (Sault et al. 1995), and performed the rest of the data reduction using the Common Astronomy Software Applications (CASA; McMullin et al. 2007). For the third epoch, we used the flux density per spectral window and mean spectral index (-0.81 ± 0.02) of 3C84 derived from the first two epochs for flux calibration. Our derived flux density values for the gain calibrator in the third epoch are consistent at all spectral windows with the values obtained from the first two epochs, where Uranus was available as a flux calibrator. We summarize

our mm-band observations in Table 4.

2.4. Centimeter: VLA

We observed the afterglow using the Karl G. Jansky Very Large Array (VLA) starting 0.45 d after the burst. We detected and tracked the flux density of the afterglow from 1.2 GHz to 33.5 GHz over seven epochs until 89 d after the burst, when it faded beyond detection at all frequencies. We used 3C48 as the flux and bandpass calibrator and J0205+3212 as gain calibrator. We carried out data reduction using CASA, and list the results of our VLA observations in Table 4.

3. BASIC CONSIDERATIONS

3.1. Optical and X-rays

The X-ray light curve exhibits a steep decline followed by flaring behavior until the first *Swift* orbital gap beginning at 1.7×10^{-2} d. Such flaring behavior in the early X-ray light curve is often attributed to prolonged central engine activity (Burrows et al. 2005a), and we therefore do not consider it further in the context of the afterglow. The subsequent X-ray light curve exhibits a flare or re-brightening event at ≈ 0.26 d, where the light curve rises steeply by a factor of ≈ 4 between 0.13 and 0.26 d, corresponding to a rise rate¹³, $\alpha = 2.0 \pm 0.3$. Such late-time flares and re-brightenings are less common in GRB X-ray light curves (Curran et al. 2008; Bernardini et al. 2011) and have variously been ascribed to instabilities in the accreting system (Perna et al. 2006; Kumar et al. 2008; Rosswog 2007), magnetic field-driven turbulence (Proga & Zhang 2006), magnetic reconnection (Giannios 2006) or by energy injection due to low-Lorentz factor ejecta (Margutti et al. 2010b; Hascoët et al. 2012; Xin et al. 2012; Laskar et al. 2015).

In the scenario where the XRT data at 0.26 d are dominated by a flare, a fit to the X-ray light curve between 0.04 and 4.0 d ignoring the flare yields a power law decay rate of $\alpha_X = -0.80 \pm 0.12$. Interpolating the X-ray light curve using this value to 0.58 d (the time of the first RATIR optical/near-IR observation; Butler et al. 2014b,a) yields a flux density of $F_{\nu,X}(0.58 \text{ d}) = (4.8 \pm 1.0) \times 10^{-5} \text{ mJy}$ (Figure 1). On the other hand, assuming that the XRT data at 0.26 d are part of a re-brightening event (and dominated by afterglow emission), a fit to the light curve at $\gtrsim 0.24$ d yields a decay rate of $\alpha_X = -1.5 \pm 0.1$ with an interpolated flux density of $F_{\nu,X}(0.58 \text{ d}) = (12.9 \pm 1.4) \times 10^{-5} \text{ mJy}$.

We plot these interpolated X-ray flux density measurements together with the RATIR optical and near-IR (NIR) observations at 0.58 d in Figure 2. A power law fit to the four longest wavelength RATIR observations (*zYJH*) after correction for Galactic extinction yields a spectral index of $\beta_{\text{NIR-opt}} = -0.98 \pm 0.20$. The flux density in the r' and i' bands is considerably lower than the extrapolation of this power law, consistent with intergalactic medium (IGM) absorption given the redshift of $z = 5.283$. In comparison, the spectral index between the RATIR H -band measurement and the interpolated X-ray flux density is $\beta_{\text{NIR-X}} = -0.96 \pm 0.02$ or $\beta_{\text{NIR-X}} = -1.09 \pm 0.03$. The X-ray spectral index,

¹³ We employ the convention, $F_\nu \propto t^\alpha \nu^\beta$ throughout.

Table 3
Optical Observations of GRB 140304A

Δt (d)	Observatory	Instrument	Filter	Frequency (Hz)	Flux density (mJy)	Uncertainty [†] (mJy)	Detection? 1=Yes	Reference
9.49×10^{-4}	ICATE	MASTER	CR	4.56×10^{14}	7.70×10^{-1}	1.56×10^{-1}	1	Gorbovskoy et al. (2014b)
1.99×10^{-3}	ICATE	MASTER	CR	4.56×10^{14}	4.64×10^{-1}	9.38×10^{-2}	1	Gorbovskoy et al. (2014b)
3.40×10^{-3}	ICATE	MASTER	CR	4.56×10^{14}	2.32×10^{-1}	4.70×10^{-2}	1	Gorbovskoy et al. (2014b)
...

Note. — [†]An uncertainty of 0.2 AB mag is assumed where not provided. The data have not been corrected for Galactic extinction. This is a sample of the full table available on-line.

Table 4
GRB 140304A: Log of radio observations

Δt (d)	Facility	Frequency (GHz)	Flux density (mJy)	Uncertainty (mJy)	Det.?
0.45	VLA	4.9	0.036	0.012	1
0.45	VLA	7.0	0.073	0.011	1
0.54	CARMA	85.5	0.656	0.235	1
...

Note. — The last column indicates a detection (1) or non-detection (0). This is a sample of the full table available on-line.

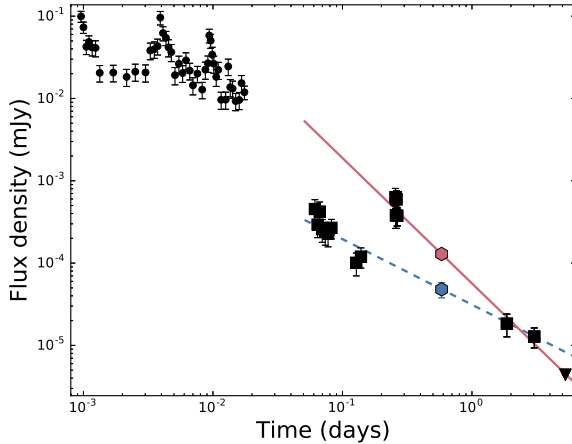


Figure 1. *Swift* XRT light curve of GRB 140304A at 1 keV (black points). Data before 0.02 d are dominated by flaring activity, while after the first orbital gap (starting at 0.02 d) the light curve exhibits a large flare / re-brightening event at 0.26 d. The lines are fits to data from 0.2 to 4.0 d (red) and from 0.04 to 4.0 d excluding the flare (blue). The latter would require an additional break at ≈ 4 d to account for the upper limit at 5.3 d. The colored points at 0.58 d are the inferred interpolated flux density at 0.58 d from the two power law fits, derived for the purpose of comparing with multi-wavelength RATIR observations at this time (Section 3.1 and Figure 2).

$\beta_X = -1.29 \pm 0.25$ is marginally steeper, suggesting a break frequency may lie between the optical and X-rays.

RATIR claimed a second detection of the optical afterglow in z' -band at 1.5 d at low significance (4.9σ). We note that the measured flux density is greater than the upper limit in the adjacent Y-band in the same epoch. Assuming this second z' -band detection is real, the decay rate between 0.58 d and 1.59 d in this band is $\alpha_z = -1.3 \pm 0.2$. On the other hand, the constraints on the decay rate from the other bands with a detection at 0.58 d are $\alpha_i \lesssim -1.8$, $\alpha_Y \lesssim -1.6$, $\alpha_J \lesssim -1.4$, and

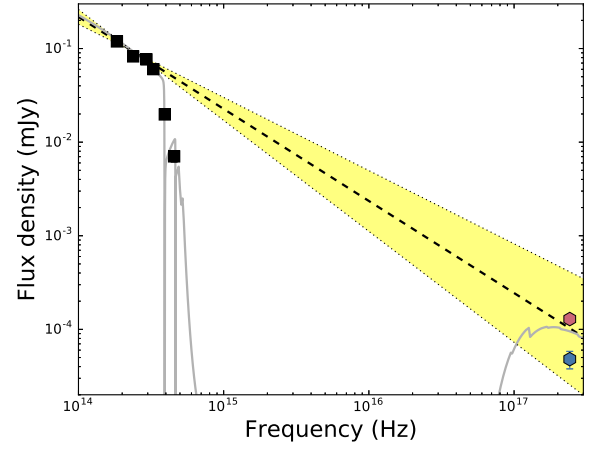


Figure 2. NIR to X-ray spectral energy distribution of the afterglow of GRB 140304A at 0.58 d. The NIR and optical data (black points) are from RATIR (Butler et al. 2014b), while the X-ray data (red and blue points) have been interpolated using two different fits to the *Swift* XRT light curve (Figure 1). The dashed line and the shaded regions indicate the best fit power law to the RATIR $zYJH$ data and its 1σ error bound. The X-ray to NIR SED is consistent with a single power law, though the X-ray spectrum suggests the cooling frequency may be located between the NIR and X-ray bands at 0.58 d. The grey solid line is the best-fit model (Section 4.2).

$\alpha_H \lesssim -1.5$. Further analysis requires a simultaneous understanding of the radio light curves, and we return to this point in Section 4.

3.2. Radio

We now discuss the radio SED at each epoch from 0.45 d to 89 d. The radio emission is expected to arise from a combination of FS radiation from the interaction of the relativistic GRB ejecta with the circumburst environment, and RS radiation from within the ejecta itself. Whereas the FS continually accelerates electrons, resulting in radio spectra comprising smoothly joined broken power law components, radiation from the RS arises from a cooling population of electrons and declines exponentially above the so-called cut-off frequency. Motivated by these physical possibilities, we fit the data with a combination of the following models in each instance wherever data quality allows:

Model 1 – Broken power law:

$$F_\nu = F_b \left(\frac{(\nu/\nu_b)^{-y\beta_1} + (\nu/\nu_b)^{-y\beta_2}}{2} \right)^{-1/y}. \quad (1)$$

This model has the property that $F_\nu(\nu_b) = F_b$; how-

Table 5
Radio spectral fits for GRB 140304A

ΔT (days)	1.5	4.5	8.5	18.2	18.2
Ncomp	2	1	2	1 [§]	2 [§]
Type [†]	exp	exp	exp	bpl	exp
ν_{peak} (GHz)	6.6 ± 0.4	21.9 ± 1.6	8.5 ± 0.3	15.6 ± 3.2	4.5 ± 0.8
F_{peak} (mJy)	0.25 ± 0.01	0.33 ± 0.02	0.143 ± 0.005	0.086 ± 0.007	0.058 ± 0.07
β_1	2.5 [‡]	2.5 [‡]	2.5 [‡]	0.45 ± 0.18	2.5 [‡]
β_2	-1.7 ± 1.0	...
y	3.0 [‡]	...
Type [†]	exp	...	exp	...	bpl
ν_{peak} (GHz)	69 ± 13	...	36.9 ± 2.1	...	11.9 ± 1.1
F_{peak} (mJy)	0.76 ± 0.20	...	0.226 ± 0.006	...	0.09 ± 0.01
β_1	2.5 [‡]	...	2.5 [‡]	...	2.5 [‡]
β_2	-1.1 [‡]
y	3.0 [‡]

Note. — [§]The SED at 18.2 d can be fit with one or two components. [†]Type = ‘bpl’ indicates a broken power law model (equation 1), and type = ‘exp’ indicates an exponential cut-off model (equation 2). [‡]Held fixed.

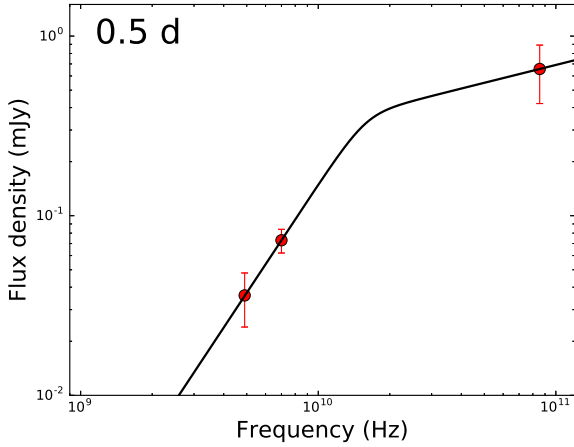


Figure 3. Radio SED of GRB 140304A at 0.5 d with a single broken power law fit. The low- and high-frequency spectral indices are fixed at 2 and 1/3, respectively (Section 3.2.1).

ever, the exact location of the peak (where $\partial F_\nu / \partial \nu = 0$) depends on β_1 and β_2 .

Model 2 – Power law with exponential cut-off:

$$F_\nu = F_b \left(\frac{\nu}{\nu_b} \right)^{\beta_1} e^{\beta_1(1-\nu/\nu_b)}. \quad (2)$$

This model has the properties that $F_\nu(\nu_b) = F_b$ and $\frac{\partial F_\nu}{\partial \nu}|_{\nu_b} = 0$.

3.2.1. SED at 0.45 d

Rapid response observations at the VLA and CARMA yielded C-band (5 and 7 GHz) and 85.5 GHz detections of the afterglow at 0.45 d (1.7 h in the rest frame). The 5 GHz to 7 GHz spectral index is steep, $\beta = 2 \pm 1$, while the 7 GHz to 85.5 GHz spectrum is shallower, $\beta = 0.9 \pm 0.2$. We fit the data at 0.5 d with a broken power law model (model 1; equation 1), with the spectral indices fixed at $\beta = 2$ at low frequencies. We note that the data do not allow us to constrain both the high frequency spectral index and the location of the spectral break simultaneously. We set the high-frequency spec-

tral index to $\beta = 1/3$, corresponding to the optically thin low-frequency tail of synchrotron emission from shock-accelerated electrons, and fix the smoothness, $y = 5$. In the best fit model (Figure 3), the spectral break occurs at 16 GHz and a flux density of 0.24 mJy with uncertainty $\approx 10\%$, dominated by the uncertain value of y .

3.2.2. SED at 1.5 d

We sampled the afterglow radio spectrum at 11 approximately evenly logarithmically-spaced frequencies spanning 5 GHz to 90 GHz with the VLA and CARMA at 1.5 d, yielding the most detailed spectral radio coverage of any GRB radio afterglow at the time of acquisition. The SED at 1.5 d exhibits two emission peaks, a feature unexpected in GRB radio afterglows. The spectral index between 5 GHz and 7 GHz remains steep, with $\beta = 1.0 \pm 0.2$.

We fit the spectrum with a sum of two exponential cut-off models (each model 2; equation 2). To account for the steep spectral index at the lower frequency end of both observed peaks in the spectrum, we fix the model spectral index at $\beta = 2.5$ for both components. The peak frequencies in our best fit model are located at (6.6 ± 0.4) GHz and (69 ± 13) GHz, with flux densities of (0.25 ± 0.01) mJy and (0.76 ± 0.20) mJy, respectively (Figure 4). We summarize these results in Table 5.

3.2.3. SED at 2.5 d

Only C-band data were obtained at 2.5 d due to a scheduling constraint. The afterglow was only marginally-detected in the upper side band (7 GHz; Figure 4), implying that the emission component creating the spectrum peak at 6.4 GHz had faded away by 2.5 d with a decline rate, $\alpha \approx -3$.

3.2.4. SED at 4.5 d

We obtained another VLA radio SED spanning 1.4 GHz to 40 GHz at 4.5 d, the mm-band afterglow having faded beyond the detection limit of CARMA. No source was detected at L-band (1.4 GHz), while the remainder of the radio SED exhibits a steep low-frequency spectrum and a clear single peak. The data can be fit with a single broken power law model with $\beta_1 = 2.5$

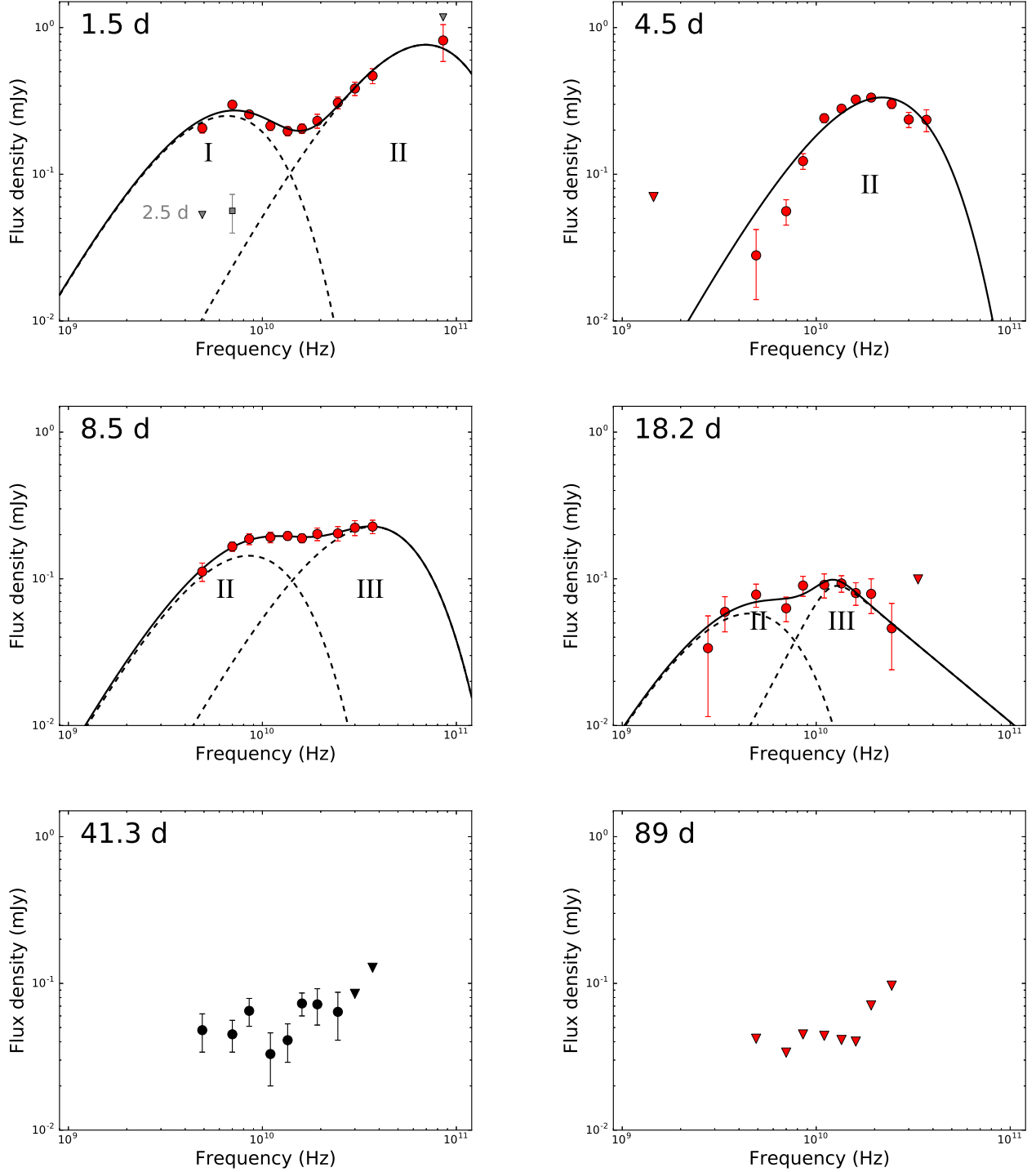


Figure 4. Radio SEDs of GRB 140304A (red points) at four epochs. Top left – SED at 1.5 d with sum of two power law plus exponential cut-off models (Section 3.2.2). Also shown are the available radio data at 2.5 d (grey square and upper limits; Section 3.2.3). Top right – SED at 4.5 d with a broken power law fit (Section 3.2.4). Center left – SED at 8.5 d with sum of two power law plus exponential cut-off models (Section 3.2.5). Center right – SED at 18.2 d with sum of a power law plus exponential cut-off and broken power law model. The high-frequency spectral index of the higher frequency component is not well constrained; the model shown here is plotted with $\beta_2 = -1.1$ and $y = 3$ (Section 3.2.6). The low-frequency spectral index is fixed at 2.5 for both components in all four epochs from 1.5 d to 18.2 d. Bottom panel – SEDs at a mean time of 41.3 d (left) and 89 d (right; Section 3.2.7).

(fixed), $\beta_2 = -0.69 \pm 0.39$, $\nu_b = (14 \pm 1)$ GHz, and $F_b = 0.30 \pm 0.02$ mJy (Figure 4).

3.2.5. SED at 8.5 d

Our next full radio SED at 8.5 d spanning 4.9 GHz to 40 GHz yields a spectrum that rises steeply from 4.9 GHz to 7 GHz, with $\beta = 1.1 \pm 0.4$ and exhibits a plateau to 40 GHz, with marginal evidence for two components. We fit the spectrum with a sum of two exponential cut-off models, fixing the slopes of the power law components at $\beta = 2.5$. The peak frequencies in our best fit model are located at 8.5 ± 0.3 GHz and 37 ± 2 GHz, with flux densities of (0.143 ± 0.005) mJy and (0.226 ± 0.006) mJy, respectively (Figure 4).

3.2.6. SED at 18.2 d

Due to the faintness of the radio emission, the VLA SED at 18.2 d can be fit with a variety of different models. We present a fit with a sum of a cut-off power law model and a broken power law model in Figure 4, fixing the lower-frequency slopes of both components at $\beta = 2.5$. Since the high-frequency spectral index of the higher frequency component (β_2) and the smoothness of the break (y) are not well constrained, we fix $\beta_2 = -1.1$ and $y = 3$. The peak frequencies in this model are located at 4.4 ± 0.9 GHz and 11.8 ± 1.2 GHz, with flux densities of (0.056 ± 0.08) mJy and (0.086 ± 0.009) mJy, respectively.

3.2.7. SEDs at 41.3 d and 89 d

The final two epochs of VLA radio observations comprise radio spectra sampled at 8–10 approximately evenly logarithmically-spaced frequencies spanning 5 GHz to 35 GHz. The afterglow fades from the previous epoch at 18.2 d to 41.3 at all observed radio frequencies. The large error bars at 41.3 d do not allow for an unambiguous model fit. The afterglow was not detected at any observing frequency in the final epoch at about 89 d. We include the observed SEDs at these last two epochs in Figure 4.

3.3. Radio light curves

The multiple components observed in the radio SEDs are also evident in the light curves. The 7 GHz light curve exhibits a rapid brightening from 0.45 d followed by a fading to 4.5 d. The precise rise and decline rates are not well constrained. Simple power law fits yield a rise rate of 1.1 ± 0.1 and decline rate of -3.4 ± 0.6 , while a broken power law fit with the peak time fixed at 1.5 d yields a rise rate of ≈ 1.3 from 0.45 d to 1.5 d followed by a decline at the rate ≈ -4.1 for $y = 5$. The light curve exhibits a re-brightening from 4.5 d to 8.5 d, with rise rate ≈ 2 followed by a decline at the rate ≈ -1.1 for a broken power law fit with peak time fixed at 8.5 d and $y = 5$ (Figure 5).

On the other hand, the 13.5 GHz light curve can be fit with a single broken power law model, with a rise rate, $\alpha_{Ku,1} \approx 0.4$, decline rate, $\alpha_{Ku,2} \approx -1.0$, and break time, $t_{b,Ku} \approx 5.4$ d, for fixed smoothness, $y = 5$. The CARMA 85.5 GHz light curve exhibits modest evidence for a rise from 0.45 d to 1.5 d at the rate ≈ 0.2 ; however, the low signal-to-noise of the detections preclude a more detailed analysis.

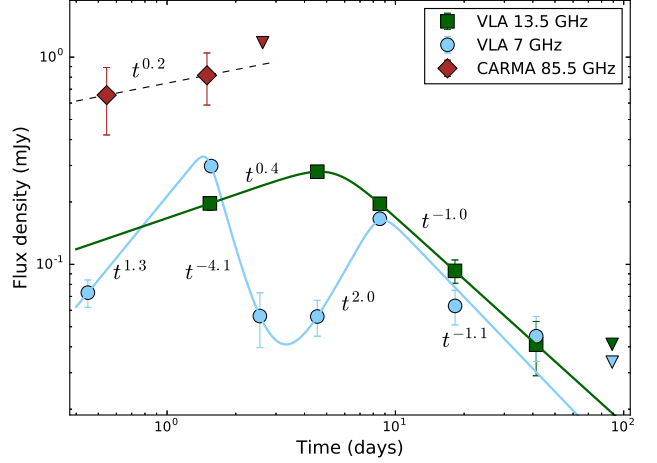


Figure 5. VLA 13.5 GHz (green) and 7 GHz (blue) light curves, together with best fit broken power law models and the resulting temporal slopes indicated. The smoothness of the breaks are fixed to $y = 5$, and the break times for the 7 GHz light curve are fixed to 1.5 d and 8.5 d, respectively. The CARMA 85.5 GHz light curve, which exhibits weak evidence for a rise, is shown for comparison (brown points).

3.4. Unexpected behavior: multiple radio components

Radio synchrotron radiation from relativistic shocks expanding adiabatically yield spectra where the peaks move to lower frequencies and fade with time (Sari et al. 1998). In this paradigm, the radio SEDs and light curves suggest that three distinct emission components contribute to the radio emission. We characterize and discuss each component in turn, followed by a critical discussion in section 5 on the physical nature of the multiple emission components.

3.4.1. Component I

Component I creates the low frequency peak in the spectrum at 1.5 d and fades rapidly, disappearing by the time of the following observations at 2.5 d (Figure 4). Since this component is not detected at any other time, its evolution cannot be further constrained in a simple manner by the radio observations; however, any model explaining this component must account for the rapid rise observed at C-band from 0.45 to 1.5 d ($\alpha \approx 1.3$), and the fast fading ($\alpha \approx -3.4$ to $\alpha \approx -4.1$) thereafter.

3.4.2. Component II

This component is identified as the high-frequency peak in the spectrum at 1.5 d. The peak of the radio emission for this component is $\nu_{pk} = 69 \pm 13$ GHz with flux density, $F_{\nu,pk} = 0.76 \pm 0.20$ mJy at 1.5 d. Component II comprises the entirety of the radio emission at 4.5 d, with a peak at 14.2 ± 0.1 GHz and flux density $F_{\nu,pk} = 0.30 \pm 0.02$, corresponding to a decline rate of -1.4 ± 0.2 in ν_{pk} and -0.8 ± 0.2 in $F_{\nu,pk}$ between 1.5 d and 4.5 d. This component additionally creates the low-frequency peak at 8.5 d ($\nu_{pk} = 8.5 \pm 0.3$ GHz) and 18.2 d ($\nu_{pk} = 4.4 \pm 0.9$ GHz), and is marked “II” in Figure 4.

Since we observe Component II at four separate epochs (1.5, 4.5, 8.5, and 18.2 d), we can fit for the temporal evolution of its peak frequency and peak flux density. If this component shares the same start time as the afterglow (we relax this assumption later), the evolution

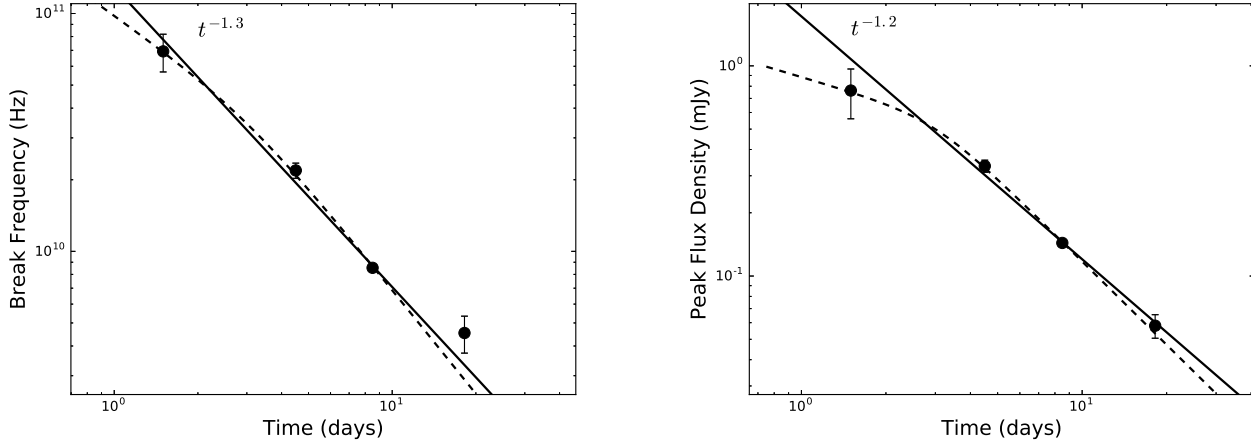


Figure 6. Evolution of the break frequency (left) and peak flux (right) of Component II in the radio SED of GRB 140304A for single power law (solid) and broken power law (dashed) models. For the broken power law fit to the evolution of the peak flux density, the break time and break sharpness have been fixed to 3 d and $y = 5$, respectively. The two models provide equally good fits for the peak frequency, and we prefer the single power law evolution for simplicity. The broken power law model is a better fit for the evolution of the peak flux; however, the break time and pre-break evolution are degenerate. Annotations in the figures refer to the single power law fits. See Section 3.4.2 for details.

of the spectral peak can be fit with a single power law, $\nu_{\text{pk}} = (1.3 \pm 0.2) \times 10^{11} t_d^{-1.25 \pm 0.08}$ Hz. A broken power law model does not significantly improve the fit for ν_{pk} . Fitting a single power law to $F_{\nu, \text{pk}}$ for all four epochs yields $F_{\nu, \text{pk}} = (1.69 \pm 0.26) t_d^{-1.15 \pm 0.07}$ mJy ($\chi^2/\text{dof} = 4.5$). A broken power law yields a better fit, but the time of this break is degenerate with the pre-break decline rate. For example, for a break time of 3 d and smoothness, $y = 5$, the best fit requires $F_{\nu, \text{pk}} \propto t^{-0.4 \pm 0.4}$ transitioning into $F_{\nu, \text{pk}} \propto t^{-1.30 \pm 0.09}$ (Figure 6).

We note that evolving ν_{pk} and $F_{\nu, \text{pk}}$ as a single power law to earlier time over-predicts the clear band flux density observed by MASTER at 9.5×10^{-4} d by a factor of 1400. Imposing a break in $F_{\nu, \text{pk}}$ leads to a discrepancy of a factor of 14. We return to this point in Section 5.3. These models do not produce significant X-ray flux. We conclude that Component II does not connect spectrally and temporally to the X-ray and optical bands, and therefore forms a distinct emission component independent of the mechanism producing the X-ray and optical radiation.

3.4.3. Component III

This component first appears in the radio SED at 8.5 d with a peak around 37 GHz and contributes the bulk of the observed flux above 10 GHz at 18.2 d. The observed SED at 41.3 d is also expected to include significant contribution from this component. Comparing the observed SEDs at 8.5 d and 18.2 d, we derive the temporal evolution of the spectral break frequency and peak flux density to be $\alpha_{\nu, \text{pk}} = -1.5 \pm 0.1$ and $\alpha_{F, \text{pk}} = -1.2 \pm 0.2$ between these two epochs, respectively. In the next section, we show that this component *does* connect with the optical and X-ray observations and therefore likely arises from the FS. The rapid decline of the peak flux density at $\gtrsim 8.5$ d suggests that a jet break occurs after 8.5 d.

3.5. Summary

To summarize, the radio data exhibit three distinct spectral components. Components I and II appear at

0.5 d – 18.2 d and do not connect with the optical and X-ray SED. We consider physical models for their origin in Section 5. Component III appears at 8.5 d at the highest cm-band frequencies (≈ 30 GHz) and likely arises from the FS.

4. SINGLE-COMPONENT MODELS

In the above discussion, we have argued for the presence of multiple spectral components in the VLA radio observations. For simplicity, we begin with a search for single-component radio models that explain the gross features of the radio SEDs and light curves in this section, and discuss multi-component radio models in Section 5. We interpret the radio observations together with the X-ray and optical/NIR data in the framework of the standard synchrotron model, where the observed SED is characterized by three spectral break frequencies – the self-absorption frequency, ν_a , the characteristic synchrotron frequency, ν_m , and the cooling frequency, ν_c – and an overall flux normalization, f_{peak} (Sari et al. 1998; Chevalier & Li 2000; Granot & Sari 2002).

Single-component radio models for GRB 140304A can be divided into two categories based on the interpretation of the X-ray light curve, in particular, the rapid re-brightening at 0.26 d. If this excess is ascribed to a flare, then the underlying X-ray light curve decline rate is $\alpha_X \approx -0.8$. Over this same period, however, the optical light curve is declining at least as steeply as $\alpha_{\text{opt}} \sim \alpha_{z'} \approx -1.3$, and perhaps as steeply as $\alpha_{\text{opt}} \sim \alpha_i \lesssim -1.8$. In the standard synchrotron model, the largest difference between α_X and α_{NIR} (when both are steeper than $\alpha = -2/3$) is $\Delta\alpha = -1/4$, which occurs on either side of the cooling frequency. It is thus impossible to arrange this scenario where a higher frequency light curve is decaying at a shallower rate than at lower frequencies, and both are declining faster than $\alpha = -2/3$, if the two light curves are dominated by radiation produced by the same shock. Thus in this situation, the X-ray and optical light curves after 0.26 d must arise from different emission regions.

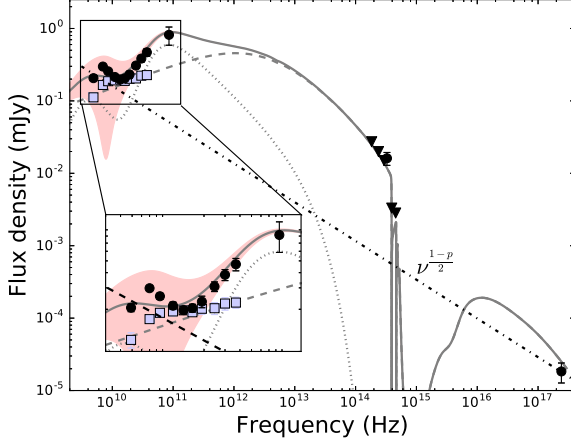


Figure 7. Radio to X-ray SED of GRB 140304A at 1.6 d (black points) and 8.5 d (blue points), with a zoom in to the radio section (inset), together with the best fit model (grey, solid), decomposed into FS (dashed) and double RS (dotted) contributions (Section 5). The dash-dot line is a single power law extrapolation from the X-ray to the radio, demonstrating that $\nu_{\text{radio}} \approx \nu_m < \nu_X < \nu_c$ with $p = 2.07$ cannot match the radio and X-ray observations (Section 4.1). In this plot, the interpolations required to plot the SED at a common time of 1.6 d are $\lesssim 10\%$ and therefore ignored.

We therefore consider two possible scenarios: (i) the X-ray excess at 0.26 d is a flare caused perhaps by extended central engine activity, while the near-IR radiation between 0.58 d and 1.59 d is produced by a different mechanism, or (ii) the X-ray and optical light curves are dominated by the FS and the X-ray excess at 0.26 d is a re-brightening of the FS radiation. We investigate both models in detail, beginning with the first scenario.

4.1. X-ray excess at 0.26 d due to flare

If we ascribe the X-ray excess at 0.26 d to a flare, the optical and X-ray emission must arise from distinct emission regions as discussed above. Under the assumption that the X-rays are dominated by the FS, the decline rate $\alpha_X = -0.8 \pm 0.12$ implies $\alpha_X =$

$$\begin{cases} \frac{2-3p}{4} \Rightarrow p = 1.73 \pm 0.16; & \nu_m, \nu_c < \nu_X \\ \frac{3(1-p)}{4} \Rightarrow p = 2.07 \pm 0.16; & \nu_m < \nu_X < \nu_c \text{ (ISM)} \\ \frac{1-3p}{4} \Rightarrow p = 1.40 \pm 0.16; & \nu_m < \nu_X < \nu_c \text{ (wind)} \end{cases} \quad (3)$$

For the standard assumption of $2 < p < 3$, the only viable scenario is the second case above; however, this model has several shortcomings. First, $\nu_X < \nu_c$ would predict $\beta_X = (1-p)/2 \approx -0.54$, which is not consistent with the observed value, $\beta_X \approx -1$. Second, if we anchor the theoretical SED to $F_X \approx 2 \times 10^{-5}$ mJy at ≈ 1.5 d and extend this spectrum to lower frequencies, we underpredict the optical by a factor of ≈ 30 , although this was already expected. Third, this model also underpredicts the CARMA detection by a factor of ≈ 80 ; in fact it is impossible to reconcile the $\nu^{(1-p)/2}$ spectrum with the radio observations without additional radio components (Figure 7).

We conclude that interpreting the X-ray excess as due to a flare would require additional components in both the optical and radio at 1.5 d. This is driven by the unexpectedly shallow decline in the X-rays, $\alpha_X \approx -0.8$

after 0.1 d, combined with a steep decline in the optical and a bright radio afterglow. Thus single-component radio models, which are the focus of this section, cannot explain the X-ray and radio observations under the assumption that the X-ray excess at 0.26 d is due to a flare.

4.2. All X-ray emission from FS

We now consider the X-ray excess to be due to a re-brightening event, possibly arising from an episode of energy injection into the FS (e.g. Sari & Mészáros 2000). In this scenario, we ignore the X-ray data before ≈ 0.2 d for the moment, and expect the X-ray and optical observations after this time to match a single FS model. We note that $\beta_X = -1.29 \pm 0.25$ is marginally different from $\beta_{\text{NIR-opt}} = -0.98 \pm 0.20$ and $\beta_{\text{NIR-X}} = -0.96 \pm 0.02$ at 0.58 d; which results in three possible scenarios: (i) $\nu_c > \nu_X$ at 0.58 d, implying $p = 1 - 2\beta \approx 3$, and predicting a common decline rate of $\alpha_X \approx \alpha_{\text{NIR}} \approx -1.5$ (ISM) or $\alpha \approx -2$ (wind). Since $\alpha_X = -1.5 \pm 0.1$, the wind model is ruled out, but the $p \approx 3$ ISM model is viable. (ii) $\nu_c < \nu_{\text{NIR}}$ at 0.58 d. This implies $p = -2\beta \approx 2$, and requires a common decline rate of $\alpha_X \approx \alpha_{\text{NIR}} \approx -1$. The steeper observed decline rate could be explained by a jet break between 0.3 and 2 d. (iii) $\nu_{\text{NIR}} < \nu_c < \nu_X$ at 0.58 d. The X-ray decline rate of $\alpha_X = -1.5 \pm 0.1$ then implies $p \approx 2.67 \pm 0.13$, predicting $\beta_X = -1.3 \pm 0.06$, $\beta_{\text{NIR}} = (1-p)/2 = -0.84 \pm 0.07$, and $\alpha_{\text{NIR}} = 3(1-p)/4 = -1.3 \pm 0.1$ (ISM) or $\alpha_{\text{NIR}} = (1-3p)/4 = -1.7 \pm 0.1$ (wind). The steeper observed spectral index in the near-IR may then be explained by a small amount of extinction in the host galaxy.

The observed X-ray and NIR spectral indices ($\beta_X = -1.29 \pm 0.25$ and $\beta_{\text{NIR}} = -0.98 \pm 0.20$) are not strongly constraining, and the model is consistent with the expected light curves in both ISM and wind scenarios. In Section 3.4.3, we showed that Component III in the radio behaves like an FS with a jet break between ≈ 8.5 and 18.2 d. Since coeval detections spanning the radio to X-ray bands only exist before ≈ 3 d where the radio SEDs exhibit multiple components, a simple determination of the location of ν_c is not straightforward. In the next section, we construct a model explaining the X-ray, near-IR, and radio light curves and SEDs under case (iii) above for the wind environment, and show that the other cases are disfavored. The remaining possibilities are presented in appendix A for completeness, and their associated figures are available in the on-line version of this article.

For a wind environment, we expect $\alpha_{\text{NIR}} = (1-3p)/4$. Thus $-1.8 \lesssim \alpha_{\text{NIR}} \lesssim \alpha_{\nu'} \approx -1.3$ implies $2.1 \lesssim p \lesssim 2.7$, which yields $-1.5 \lesssim \alpha_X \lesssim -1.1$, also consistent with observations. We find a good fit to the X-ray and optical light curves with $p \approx 2.6$ and ν_c above the NIR band (Table 6). This model fits the optical and light curves after 0.2 d well, and also captures the evolution of the radio SED after ≈ 18.2 d. Our best fit model has $\epsilon_e \approx 2.5 \times 10^{-2}$, $\epsilon_B \approx 2.9 \times 10^{-2}$, $A_* \approx 2.6 \times 10^{-2}$, and $E_{\text{K,iso}} \approx 4.9 \times 10^{54}$ erg. The model requires modest extinction, $A_V \approx 0.1$ mag, and a jet break at $t_{\text{jet}} \approx 10.6$ d, corresponding to a jet opening angle of 1.1 deg.

4.3. Energy injection into the FS

In the preceding section, we have argued that the X-ray excess at ≈ 0.26 d likely arises from a re-brightening of

Table 6
Parameters for best-fit wind model

Parameter	Value
Ordering at 0.1 d	$\nu_{\text{NIR}} < \nu_c < \nu_X$
p	2.59
ϵ_e	2.5×10^{-2}
ϵ_B	5.9×10^{-2}
A_*	2.6×10^{-2}
$E_{\text{K,iso},52}$	4.9×10^2
t_{jet} (d)	10.6
θ_{jet} (deg)	1.13
A_V (mag)	0.09
ν_a (Hz)	$3.0 \times 10^{8\dagger}$
ν_m (Hz)	2.0×10^{14}
ν_c (Hz)	6.4×10^{15}
$F_{\nu,\text{max}}$ (mJy)	4.2
E_γ (erg)	2.3×10^{49}
E_K (erg)	9.5×10^{50}
E_{tot} (erg)	9.7×10^{50}
η_{rad}	$\approx 2\%$

Note. — All break frequencies are listed at 0.1 d. \dagger These break frequencies are not directly constrained by the data.

the afterglow, rather than from late-time central engine activity. We now model the rapid rise in the X-ray light curve as energy injection into the FS using the methods described in [Laskar et al. \(2015\)](#).

Since $\nu_c < \nu_X$ at the time of the re-brightening, the X-ray flux density, $F_X \propto E^{\frac{2+p}{4}} t^{\frac{2-3p}{4}}$. The light curve rises during this period as $t^{2.0 \pm 0.3}$, which yields $E \sim t^{3.0 \pm 0.3}$. Starting with the afterglow model, we find a good fit to the re-brightening event for $E \sim t^{3.8}$ between 0.15 d and 0.26 d, close to the value expected from simple considerations. This corresponds to an increase in $E_{\text{K,iso}}$ by a factor of ≈ 8 from $E_{\text{K,iso}} \approx 6.1 \times 10^{52}$ erg at 0.15 d to $\approx 4.9 \times 10^{54}$ erg at 0.26 d. The resultant r' -band light curve¹⁴ also agrees with the MASTER optical observations between 3×10^{-3} d and 4×10^{-2} d. Our best-fit wind model is presented in Figures 8 and 9. We investigate the ISM case for the three possible locations of ν_c relative to ν_{NIR} and ν_X (as described in Section 4.2) in Appendix A, and present the associated light curves and radio SEDs in Figures 12, 13, 14, 15, 16, and 17, including the effects of energy injection. However, in each case the models significantly under-predict the optical light curve before 4×10^{-2} d, and are therefore disfavored.

To summarize, the continued high flux density of the X-ray detections after ≈ 1 d suggests that the X-ray excess at ≈ 0.26 d is not due to late-time central engine activity, but is caused by a re-brightening of the FS radiation. The multi-band data are consistent with a wind-like circumburst medium, requiring a single episode of energy injection at ≈ 0.2 d. The resultant model fits the optical and X-ray evolution and matches the radio SED after 18 d. However, this model under-predicts the CARMA

¹⁴ Given the high redshift of the GRB, $z = 5.283$, the optical r' and i' -band observations are significantly affected by IGM absorption. For our subsequent analysis, we integrate model spectra over the SDSS r' and i' bandpasses. A more detailed analysis would require knowledge of the individual response functions of each telescope and the spectra of the calibration stars used; however, this is not available and clearly beyond the scope of the present discussion.

light curve, as well as the 5–83 GHz SED at 1.5 d and 8.55 d. To account for these deficits, we next investigate the effect of including emission from additional components. We delineate the evidence for their presence, and consider their possible physical origins.

5. MULTI-COMPONENT MODELS

5.1. Reverse Shock

In Section 3.2, we discussed the apparent multi-component structure of the radio SEDs between 1.5 d and 18.2 d. In the previous section, we have shown that while a single FS model can reproduce the gross features of the radio light curves, such a model cannot explain the multiple peaks in the SED at 1.5 d, the ≈ 14 GHz peak at 4.5 d, and the SED at 8.55 d. Of these, the greatest discrepancy between data and model arises in the radio SEDs at 1.5 d and 4.55 d. We now consider whether each spectral peak at 1.5 d can in turn be ascribed to radiation from an RS.

An RS propagating into GRB ejecta is expected to produce synchrotron radiation with its own set of characteristic frequencies, $\nu_{a,r}$, $\nu_{m,r}$, and $\nu_{c,r}$, and peak flux, $F_{\nu,m,r}$. These quantities are related to those of the FS at the deceleration time, t_{dec} , when the RS just crosses the ejecta, and the relation between the two sets of break frequencies and fluxes allows for a determination of the ejecta Lorentz factor and magnetization. After the RS crosses the ejecta, the flux above $\nu_{c,r}$ declines rapidly¹⁵ as no electron is newly accelerated within the ejecta. Since no radiation is expected above $\nu_{c,r}$, a conservative lower limit to the optical light curve can be computed by taking $\nu_{c,r}$ to be located near each observed radio spectral peak at 1.5 d in turn.

For the high frequency component, this occurs in the mm band (85.5 GHz) at 1.5 d. For a wind-like circumburst environment, $\nu_{c,r} \propto t^{-15/8}$ for a relativistic RS and $\nu_{c,r} \propto t^{-(15g+24)/(14g+7)}$ for a Newtonian RS, where $1/2 \lesssim g \lesssim 3/2$ from theoretical arguments ([Mészáros & Rees 1999](#); [Kobayashi & Sari 2000](#)). Therefore, the slowest expected evolution of this break frequency is $\approx t^{-1.7}$, whereupon it would have crossed the optical r' -band at ≈ 0.01 d. The peak flux density evolves as $F_{\nu,\text{pk}} \propto t^{-(11g+12)/(14g+17)} \propto t^{-1}$. The flux density in the CARMA 85.5 GHz band at 1.5 d is ≈ 0.8 mJy, which yields a peak flux density $\gtrsim 120$ mJy at 0.01 d in the optical, which is two orders of magnitude brighter than the MASTER observations. Therefore, a regular RS cannot explain the high-frequency radio peak at 1.5 d.

The low frequency spectral peak at 1.5 d occurs at ≈ 7 GHz. Taking $\nu_{c,r} \approx 7$ GHz and $F_{\nu,m} \approx 0.25$ mJy at this time, we can show that relativistic RS models over-predict the optical flux density before $\approx 4 \times 10^{-3}$ d by two orders of magnitude and are therefore ruled out. On the other hand, a Newtonian RS with $g \approx 2.3$, $\nu_{a,r} \approx 4.2 \times 10^9$, $\nu_{c,r} \approx 7.7 \times 10^9$, and $F_{\nu,a} \approx 0.28$ mJy results in spectra and light curves that represent the data well. In this model, $\nu_{m,r} \ll \nu_{a,r}$, and is therefore unconstrained. Requiring that these values be consistent with the FS at the deceleration time (t_{dec}), we derive

¹⁵ The angular time delay effect prevents abrupt disappearance of flux above $\nu_{c,r}$; instead, we expect $F_{\nu > \nu_{c,r}} \propto t^{-\frac{p+4}{2}} \approx t^{-3.3}$ ([Kobayashi & Zhang 2003](#)).

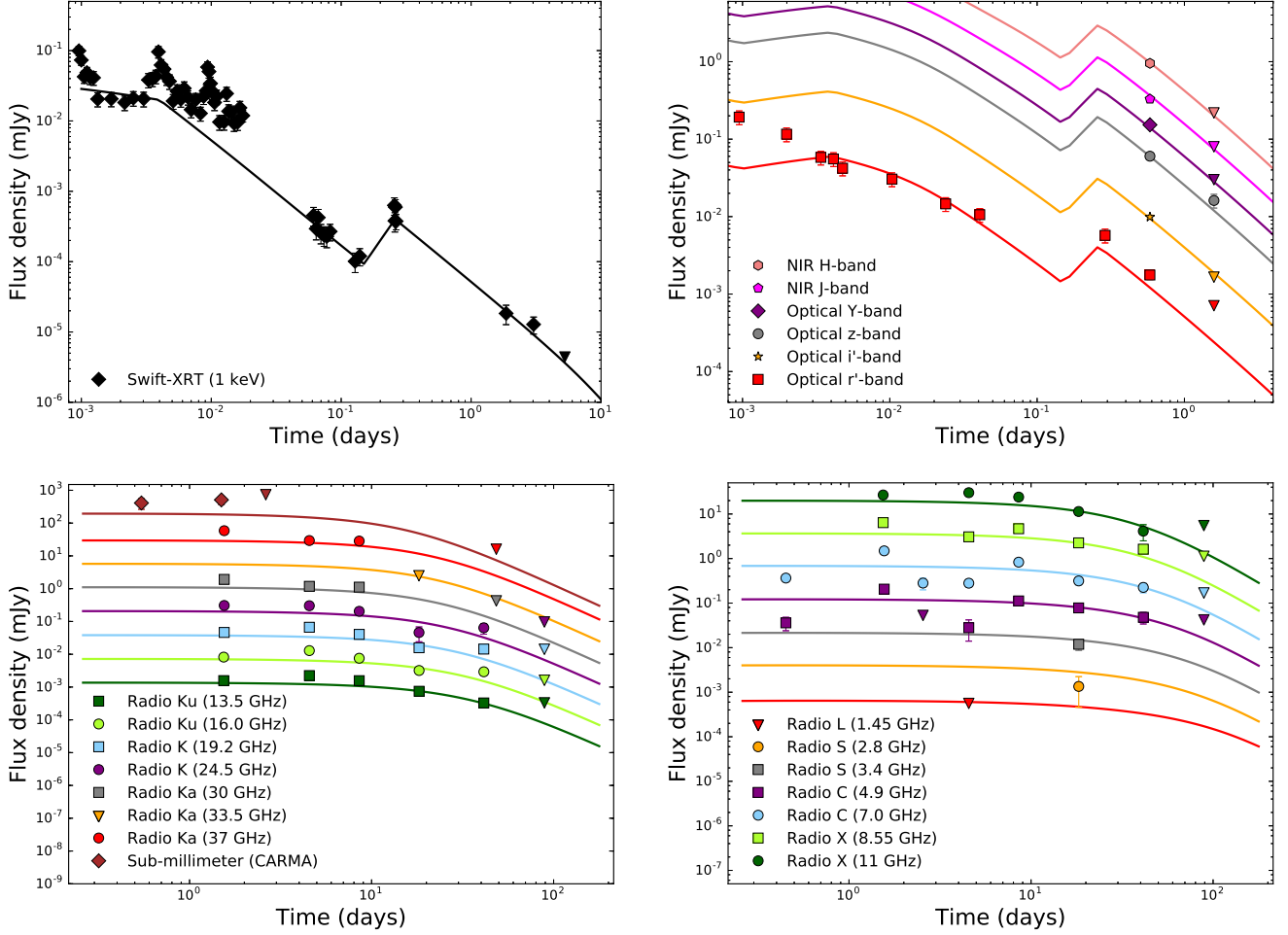


Figure 8. X-ray (top left), optical/NIR (top right) and radio (bottom) light curves of the afterglow of GRB 140304A, together with a FS wind model, including energy injection between 0.15 d and 0.26 d (Section 4.3). The model matches the X-ray light curve after 5×10^{-2} d, the optical observations, and the overall features of the radio light curves.

$t_{\text{dec}} \approx 1.2 \times 10^{-3}$ d (≈ 100 s $\approx 6T_{90}$), the Lorentz factor at the deceleration time, $\Gamma(t_{\text{dec}}) \approx 300$, and the RS magnetization, $R_B \equiv \epsilon_{B,\text{RS}}/\epsilon_{B,\text{FS}} \approx 0.6$. Here, t_{dec} is constrained to be between the first two MASTER observations in order to not over-predict the flux at either time. Whereas our derived value of g is higher than the theoretically expected bounds for a wind environment, we note that previous studies have found even higher values from observations and modeling of GRB 130427A (Laskar et al. 2013; Perley et al. 2014). The critical Lorentz factor separating the thick and thin shell regimes is given by

$$\Gamma_{\text{crit}} = 88 \left[\frac{(1+z)A_*}{E_{K,\text{iso},52}T_{90}} \right]^{1/4}, \quad (4)$$

with $\Gamma < \Gamma_{\text{crit}}$ corresponding to the thin shell and Newtonian RS regime (Kobayashi et al. 2004). For the FS parameters in Table 6, $\Gamma_{\text{crit}} \approx 690$ and $\Gamma(t_{\text{dec}}) < \Gamma_{\text{crit}}$ as required; however, we caution that $\Gamma(t_{\text{dec}})$, R_B , and t_{dec} are all degenerate with respect to $\nu_{\text{m,r}}$ in this model.

Before t_{dec} , the FS is expected to increase in energy as the ejecta energy is transferred to the FS. A complete description of this process requires knowledge of the ejecta Lorentz factor distribution and numerical simulations;

however, for a single shell this process can be approximated by linear energy injection $E \propto t$ (see Appendix B), which yields a constant blast wave Lorentz factor akin to the coasting phase of jet evolution (Duffell & MacFadyen 2015). We plot the resulting light curves and radio SEDs in Figures 10 and 11, respectively.

5.2. Interstellar Scintillation

We note that detailed analysis for the low-frequency radio spectral component at 1.5 d is challenging due to the increased contribution of interstellar scintillation (ISS) expected at frequencies below ≈ 10 GHz from the Milky Way interstellar medium (ISM). It is possible that the entirety of this component is caused by an upward fluctuation due to ISS. The correlation bandwidth for diffractive ISS is given by,

$$\Delta\nu_D \approx 2.8 \times 10^8 (\nu/5 \text{ GHz})^{4.4} \text{ GHz}, \quad (5)$$

toward this line of sight (Goodman & Narayan 2006). This is of the same order as the observing bandwidth, ≈ 1 GHz. The diffractive scintillation time scale,

$$t_{\text{diff}} \approx 80 (\nu/5 \text{ GHz})^{1.2} (v_{\perp}/30 \text{ km s}^{-1})^{-1} \text{ min}, \quad (6)$$

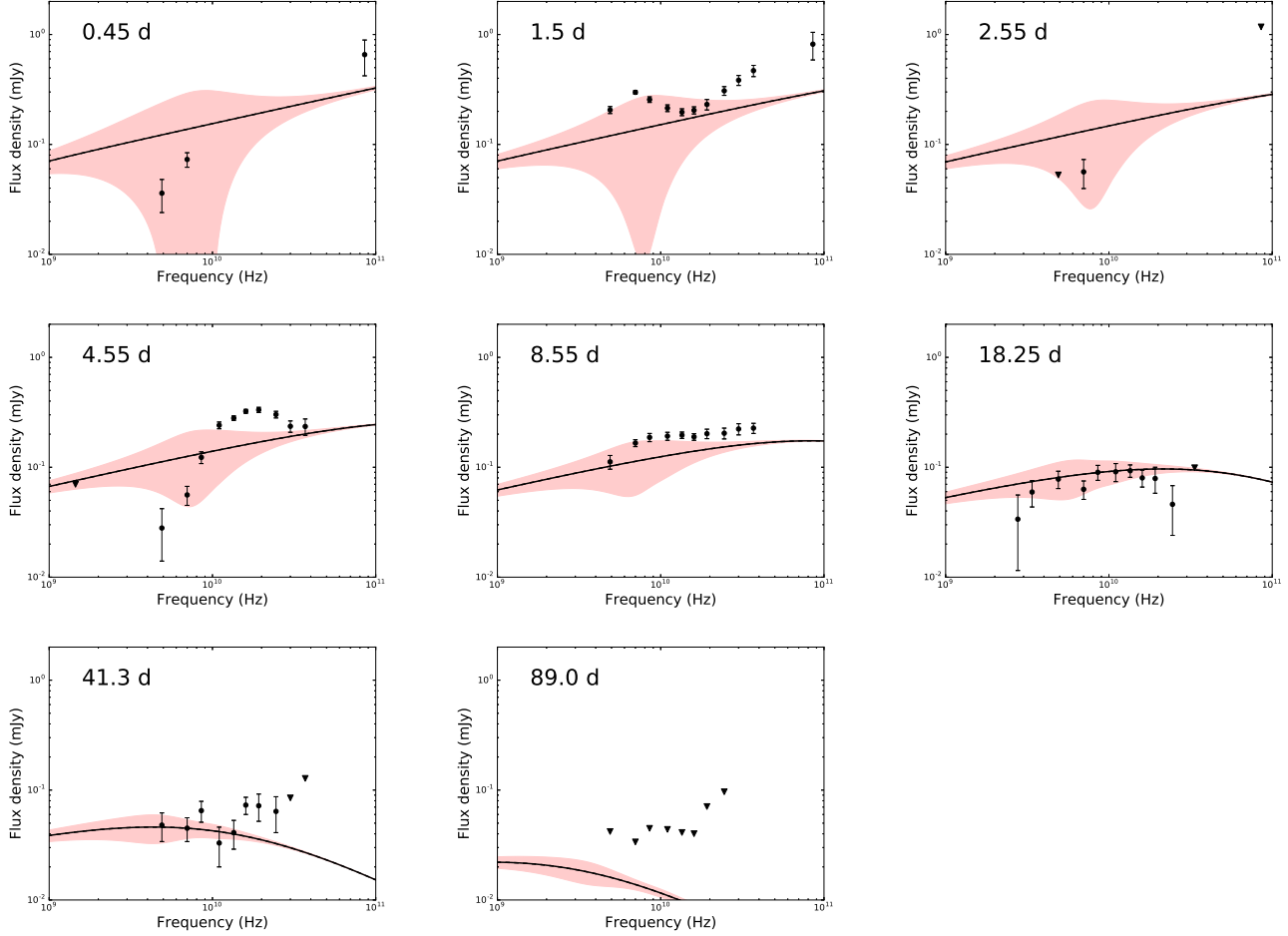


Figure 9. Radio spectral energy distributions of the afterglow of GRB 140304A at multiple epochs starting at 0.45 d, together with the same FS wind model in Figure 8. The red shaded regions represent the expected variability due to scintillation. The model captures the evolution after 18.25 d, but under-predicts the mm-band data and the observations above ≈ 10 GHz before 8.55 d.

where v_{\perp} is the perpendicular velocity of the Earth relative to the line of sight. Here we have taken the distance to the scattering screen of $d_{\text{scr}} = 1.1$ kpc for a transition frequency of $\nu_T \approx 11.6$ GHz and a scattering measure, $\text{SM} = 3.5 \times 10^{-4} \text{ kpc m}^{-20/3}$ from the Galactic electron density model, NE2001 (Cordes & Lazio 2002). Our C-band and X-band observations at 1.5 d span ≈ 20 min each. We attempted to test for short-time scale variability by imaging each scan individually¹⁶. The results do not reveal significant variability, suggesting that either the observed spectral feature at 1.5 d is intrinsic to the source, or the variability time scale is significantly longer than probed by our observations. Our subsequent analysis incorporates the expected contribution of both diffractive and refractive scintillation as described in Laskar et al. (2014).

5.3. Reverse Shock from a shell collision

We note that our multi-wavelength analysis in Section 4.2 indicates a period of significant energy injection between 0.15 d and 0.26 d. During this interval, the observed rate of energy increase ($E \propto t^{3.8}$) is greater than can be achieved from the gentle interaction of ejecta

shells with a simple power law distribution of Lorentz factor. In particular, for injection due to ejecta mass distribution of $M(> \Gamma) \propto \Gamma^{-s+1}$, the energy of the FS increases as $E \propto t^m$, where $m = (s-1)/(s+3) < 1$. However, if the increase in energy is due to a violent interaction of two colliding shells, a greater rate of energy increase is feasible (Lyutikov 2017; Lamberts & Daigne 2017). Such an interaction would generate a RS propagating into the second shell and contribute to the observed synchrotron radiation.

Since the energy injection at 0.15 d is rapid, we expect an RS to form at this time, which propagates through the second shell while the injection process continues. After the injection ends at 0.26 d, radiation from the shock is expected to fade as the shocked ejecta expand and cool due to synchrotron and adiabatic losses. In Figures 10 and 11, we present a model with an additional Newtonian RS that is launched at a collision time of $t_{\text{col}} \approx 0.15$ d, and propagates through the ejecta until the end of injection at 0.26 d. This model requires $\nu_{a,r} \approx 60$ GHz, $\nu_{c,r} \approx 2 \times 10^{13}$ Hz, $g \approx 2$, and $F_{\nu,a} \approx 1.3$ mJy, with $\nu_{m,r} \ll \nu_{a,r}$. For this value of g , $\nu_c \sim t_x^{-1.5}$ and $F_{\nu,\text{pk}} \sim t_x^{-1}$, where $t_x = t - t_{\text{col}}$, which agree well with the basic properties of Component II derived in Section 3.4.2.

¹⁶ The scan length is 510 s at C band and 309 s at X band.

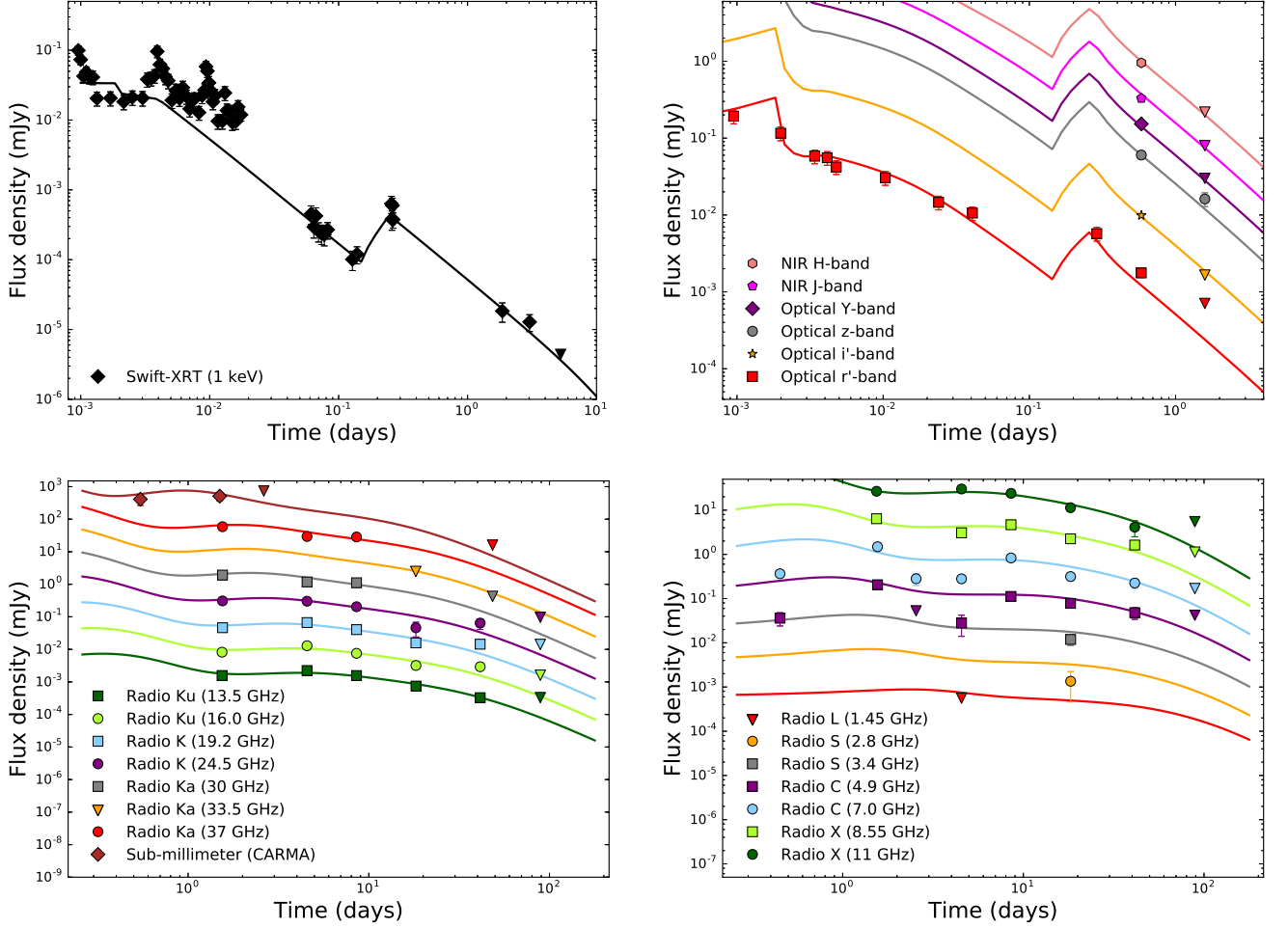


Figure 10. Same as Figure 8, now including energy injection between 0.15 d and 0.26 d (Section 4.3), a standard RS contributing to the optical/NIR light curve before 2×10^{-3} d and to the radio at 1.5 d (Section 5.1), and a refreshed RS contributing to the mm-band light curve (Section 5.3).

The Lorentz factor of the second shell is then given by,

$$\Gamma_2 = 2^{1/2} \Gamma_1 \left(1 - \frac{\Delta t_L}{t_{\text{col}}} \right)^{-1/2}, \quad (7)$$

where Γ_1 is the Lorentz factor of the FS at the time of collision and Δt_L is the interval in the observer frame between the ejection of the two shells (Appendix C). From the energy injection model, $t_{\text{col}} \approx 0.15$ d. From the Blandford & McKee (1976, BM) solution, $\Gamma_1 \approx 110$ for the FS at this time for the parameters derived in Section 4.2. The two quantities Δt_L and Γ_2 are degenerate – a shell emitted at a later time may catch up at the same collision time, t_{col} if Γ_2 is higher. We can break this degeneracy by invoking additional information from the X-ray light curve. If we suppose the X-ray flaring activity up to $\approx 10^{-2}$ d is related to the ejection of this second shell, then we determine $\Gamma_2 \approx 160$. While this computation relies on several assumptions, we note the resulting Lorentz factor is lower than $\Gamma(t_{\text{dec}}) \approx 300$ for the ejecta derived in Section 5.1.

6. SUMMARY AND DISCUSSION

We present detailed multi-frequency, multi-epoch radio observations of GRB 140304A at $z = 5.283$ span-

ning 1 GHz to 86 GHz and 0.45 d to 89 d. The radio and mm SEDs comprise at least three distinct spectral components. We investigate physical models responsible for each emission component through detailed multi-wavelength analysis in the standard synchrotron emission paradigm.

The first component may arise either from extreme scintillation, or from a Newtonian RS propagating through the first ejecta shell. In the latter case, we derive a Lorentz factor of $\Gamma(t_{\text{dec}}) \approx 300$, a deceleration time, $t_{\text{dec}} \approx 1.2 \times 10^{-3}$ d, and weak ejecta magnetization, $R_B \approx 0.6$. However, these parameters are degenerate with respect to the unknown value of the characteristic frequency, $\nu_{\text{m,r}}$, which is located below the radio band at all times.

The second component is consistent with emission from a refreshed RS produced by the violent collision of two shells with different Lorentz factors emitted at different times. The collision injects energy into the FS, which manifests as a re-brightening in the X-ray light curve. The initial Lorentz factor of the second shell is degenerate with its launch time; if the flaring activity observed in the X-ray light curve is associated with the creation of this shell, we can break this degeneracy and obtain $\Gamma \approx 160$.

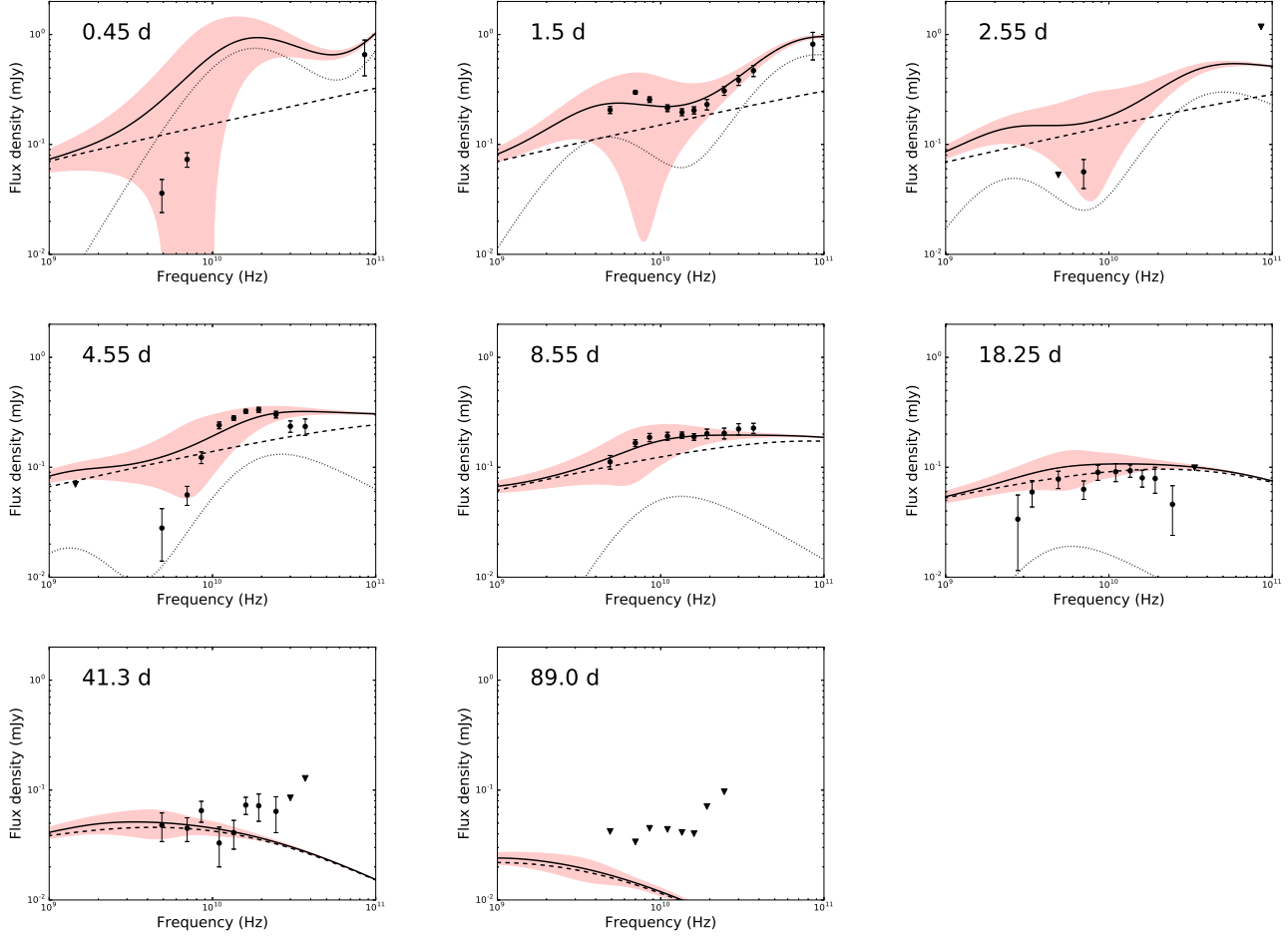


Figure 11. Same as Figure 9, but for the model (solid) shown in Figure 10 decomposed into FS (dashed) and RS (dotted) contributions. The two RS components are best distinguished at 1.5 d, where the lower frequency component arises from a RS in the original shell producing the GRB, while the higher frequency component arises from the collision of two shells at 0.15 d, which also produces the X-ray re-brightening. The red shaded regions represent the expected variability due to scintillation.

The third component is consistent with synchrotron radiation from a forward shock propagating into a wind medium with $A_* \approx 2.6 \times 10^{-2}$, corresponding to a progenitor mass loss rate of $\dot{M} \approx 3 \times 10^{-7} M_\odot \text{ yr}^{-1}$ for a wind velocity of 1000 km s^{-1} . The total energy of the ejecta inferred from modeling the FS using the X-ray, optical/NIR and radio observations after 0.26 d is $E_{K, \text{iso}} \approx 5 \times 10^{54} \text{ erg}$. The inferred prompt efficiency derived by comparing E_γ with the final ejecta kinetic energy is low, $\eta \approx 2\%$. However, the true prompt efficiency is expected to be related to the energy of the first shell, $E_{K, \text{iso}} \approx 6 \times 10^{53} \text{ erg}$. Assuming this shell is responsible for the prompt γ -rays, we obtain a prompt efficiency of $\eta \approx 17\%$, commensurate with the internal shock model (Kobayashi et al. 1997). The radio observations suggest a jet break at $\approx 11 \text{ d}$, yielding a narrow jet opening angle of $\theta_{\text{jet}} \approx 1.1 \text{ deg}$. The small opening angle is in accordance with our previous work showing evidence of a narrower median opening angle for GRBs at $z \gtrsim 6$ compared to events at lower redshift (Laskar et al. 2014). The resulting beaming-corrected energies are $E_K \approx 10^{51} \text{ erg}$ and $E_\gamma \approx 2 \times 10^{49} \text{ erg}$.

The proposed model matches the X-ray, optical, NIR, and radio observations over five orders of magnitude in

time from 10^{-3} d to 89 d . For completeness, we have considered alternate scenarios that do not invoke multiple radio components. However, no scenario can simultaneously explain the X-ray re-brightening, together with the observed optical and radio evolution as well as the three-component radio SEDs.

7. CONCLUSIONS

The bright radio afterglow of GRB 140304A has yielded unexpected riches: the presence of multiple radio spectral components and a late-time X-ray re-brightening. Together with optical observations, the radio components are suggestive of multiple shocks partly arising from a period of energy injection initiated by the collision of two relativistic shells. Whereas the details of the radio SEDs cannot be perfectly matched even with multiple emission components, the residual offsets are consistent with an origin in interstellar diffractive scintillation. These observations highlight the importance of disentangling the effects of scintillation from intrinsic physical processes, a process that is challenging given the current uncertainty in scintillation theory. Further multi-frequency observations of GRB afterglows in the cm and mm-bands, coupled with advances in scintilla-

tion theory will be key to a detailed understanding of these new physical effects.

We thank Paul Duffell for helpful discussions. TL is a Jansky Fellow of the National Radio Astronomy Observatory. The Berger Time-Domain Group at Harvard is supported in part by the NSF under grant AST-1411763 and by NASA under grant NNX15AE50G. BAZ acknowledges support from NSF AST-1302954. VLA observations for this study were obtained via project 14A-344. The National Radio Astronomy Observatory is a facility of the National Science Foundation operated under cooperative agreement by Associated Universities, Inc. This research has made use of data supplied by the UK Swift Science Data Centre at the University of Leicester, and of data obtained through the High Energy Astrophysics Science Archive Research Center On-line Service, provided by the NASA/Goddard Space Flight Center.

APPENDIX

A. ADDITIONAL FORWARD SHOCK-ONLY MODELS

In the main text, we show that the radio to X-ray emission of the afterglow is consistent with FS and RS radiation in a wind-like circumburst environment. We present ISM models here for completeness. There are three possible scenarios depending on the location of ν_c relative to ν_{NIR} and ν_X as discussed in Section 4.2, and we describe each in turn. The resulting best-fit parameters are summarized in Table 7. The figures and tables associated with these models are available in the on-line version of the journal. We note that these models significantly underpredict the r' -band light curve before ≈ 0.1 d and are therefore disfavored¹⁷.

A.1. High cooling frequency, $\nu_c > \nu_X$

If $\nu_m < \nu_{\text{NIR}} < \nu_X < \nu_c$, we require $p \approx 2.9$ to explain the optical/NIR and X-ray light curves (Section 4.2). The resulting model fits the X-ray and NIR observations after 0.2 d, and the radio SED at 8.5 d and 18.25 d. However, it over-predicts the 4.9 GHz flux density and under-predicts the CARMA observation at 0.45 d, results in an excess at ≈ 15 GHz at 1.5 d, severely over-predicts the 4.9 and 7.0 GHz data at 2.5 d, does not match the steep radio spectrum at 4.5 d, and marginally under-predicts the radio SED at 41.3 d (Figures 12 and 13). In addition, the model requires¹⁸ a very high isotropic-equivalent kinetic energy, $E_{K,\text{iso}} \approx 3 \times 10^{56}$ erg, a low density, and a very small jet opening angle, $\theta_{\text{jet}} \approx 0.5$ deg.

¹⁷ Attempting to explain the deficit as RS emission either over-predicts the data at other wavelengths or yields unrealistic parameters in conjunction with the FS model, such as $\Gamma(t_{\text{dec}}) \approx 10$.

¹⁸ Since both ν_a and ν_c are unconstrained by this model, the physical parameters can be scaled as $\epsilon_e = \epsilon_e^* (\nu_a/\nu_a^*)^{5/6} (\nu_c/\nu_c^*)^{1/4}$, $\epsilon_B = \epsilon_B^* (\nu_a/\nu_a^*)^{-5/2} (\nu_c/\nu_c^*)^{-5/4}$, $n_0 = n_0^* (\nu_a/\nu_a^*)^{25/6} (\nu_c/\nu_c^*)^{3/4}$, and $E_{K,\text{iso}} = E_{K,\text{iso}}^* (\nu_a/\nu_a^*)^{-5/6} (\nu_c/\nu_c^*)^{1/4}$ without modifying the spectrum (modulo inverse Compton corrections), where the parameters with asterisks refer to the values in Table 7. In the limit $\epsilon_e \rightarrow 1$, $E_{K,\text{iso}} \rightarrow 1.3 \times 10^{55}$ erg remains high.

A.2. Low cooling frequency, $\nu_c < \nu_{\text{NIR}}$

If both ν_m and ν_c are below ν_{NIR} , the optical/NIR and X-ray light curves do not distinguish between ISM and wind environments. In this scenario, the expected light curve decline rate is $\alpha \approx -1$. The observed decline rate is $\alpha_X \approx -1.5$ and $\alpha_{\text{NIR}} \lesssim -1.8$, which can be explained as a jet break between ≈ 0.3 and ≈ 2 d. This model matches the X-ray light curve after 0.2 d, requiring a jet break at ≈ 2.5 d. It also fits the 5–40 GHz SED at 0.45 d, 1.5 d, and after 8.5 d. However, it significantly over-predicts the 5–7 GHz observations at 2.55 d, does not match the steep spectrum below 10 GHz, and slightly over-predicts the optical/NIR limits at 1.58 d (Figures 14 and 15).

A.3. Intermediate cooling frequency, $\nu_{\text{NIR}} < \nu_c < \nu_m$

For the spectral ordering $\nu_m < \nu_{\text{NIR}} < \nu_c$ in the ISM environment, we expect $\alpha_{\text{NIR}} = 3(1-p)/4$. Since $\alpha_{\text{NIR}} \lesssim \alpha_{z'} \approx -1.3$, this requires $p \gtrsim 2.73$, which yields $\alpha_X = (2-3p)/4 \lesssim -1.55$, consistent with observations. The H -band flux density at 0.58 d corrected for Galactic extinction is $F_H = (12.3 \pm 0.9) \times 10^{-2}$ mJy. Interpolating the X-ray light curve between 0.2 d and 3 d, the X-ray flux density at this time is $F_X = (12.9 \pm 1.4) \times 10^{-5}$ mJy (Section 3.1). For $p \approx 2.73$, the spectral index on either side of the cooling frequency is $\beta = (1-p)/2 \approx -0.87$ for $\nu < \nu_c$ and $\beta = -p/2 \approx -1.36$ for $\nu > \nu_c$. This allows us to locate $\nu_c \approx 6.6 \times 10^{16}$ Hz at 0.58 d.

Fitting the gross features of the radio SED at 1.5 d as a $\nu^{1/3}$ power law, the millimeter-band ($\nu_{\text{mm}} = 85.5$ GHz) flux density at 0.58 d,

$$F_{\text{mm}}(0.58 \text{ d}) = F_{\text{mm}}(1.5 \text{ d}) \times (0.58/1.5)^{1/2} \approx 0.5 \text{ mJy.} \quad (\text{A1})$$

Requiring that this connect with the NIR SED at 0.58 d, we have

$$F_{\text{mm}} = f_{\nu,\text{max}} \left(\frac{\nu_{\text{mm}}}{\nu_m} \right)^{\frac{1}{3}} = F_H \left(\frac{\nu_m}{\nu_H} \right)^{\frac{1-p}{2}} \left(\frac{\nu_{\text{mm}}}{\nu_m} \right)^{\frac{1}{3}}, \quad (\text{A2})$$

which yields $\nu_m \approx 7 \times 10^{12}$ Hz at 0.58 d. This spectrum requires extreme parameters (low density and high energy), while ν_a remains unconstrained (Table 7). The resulting light curves and SEDs are presented in Figures 16 and 17. We note that the resulting parameters are very similar to the model described in Section A.1, the difference in the location of ν_c being offset by the slightly different value of p .

B. THE EARLY FS

The energy of the FS increases before t_{dec} , while the RS is still crossing the ejecta. During this coasting period, the Lorentz factor, Γ_0 , of the jet is approximately constant if the RS is Newtonian (Gao et al. 2013). Thus, the observer time, $t_{\text{obs}} \sim t/\Gamma_0^2 \propto t$, where t is the time in the frame in which the circumburst medium is at rest. The FS radius, $r \propto t$, and the energy density of the shocked ISM, $\varepsilon \propto \Gamma_0^2 \rho \propto r^{-k}$. The energy of the FS then increases as

$$\frac{dE}{dt} = \varepsilon 4\pi r^2 \frac{dr}{dt} \propto r^{2-k}, \quad (\text{B1})$$

and thus $E \propto r^{3-k}$. For a wind medium, this gives $E \propto r \propto t \propto t_{\text{obs}}$, and the blast wave energy increases linearly

with observer time.

C. SHELL COLLISIONS

Consider a central engine that emits two shells of Lorentz factors, Γ_1 , and Γ_2 at times $t = 0$ and $t = \Delta t$, respectively, where t is measured in the frame in which the circumburst medium is at rest. After the first shell is decelerated by the environment, its radius is given by the BM solution,

$$R_1(t) = \left[1 - \frac{1}{2(4-k)\Gamma_1(t)^2} \right] ct, \quad (\text{C1})$$

The two shells collide at a time t_1 , when the Lorentz factor of the first shell is reduced to $\Gamma_1(t_1)$, also given by the BM solution,

$$\Gamma_1(t) = \left[\frac{(17-4k)E}{8\pi A c^{-k} t^{3-k}} \right]^{1/2} \quad (\text{C2})$$

The second shell moves with a constant Lorentz factor, and its radius is given by

$$R_2(t) = c(t - \Delta t) \left(1 - \frac{1}{2\Gamma_2^2} \right) \quad (\text{C3})$$

We can take the time of collision between the shells to be when their radii are equal,

$$R_1(t_1) = R_2(t_1), \quad (\text{C4})$$

which yields

$$1 - \frac{1}{2(4-k)\Gamma_1(t_1)^2} = \left(1 - \frac{\Delta t}{t_1} \right) \left[1 - \frac{1}{2\Gamma_2(t_1)^2} \right]. \quad (\text{C5})$$

The observer time,

$$t_z = (1+z)(t - R/c) = (1+z) \frac{t}{2(4-k)\Gamma_1^2} \quad (\text{C6})$$

Thus, the collision time in the observer frame,

$$t_{\text{col}} = (1+z) \frac{t_1}{2(4-k)\Gamma_1^2}, \quad (\text{C7})$$

while the shell launch delay in the observer frame,

$$\Delta t_L = (1+z)\Delta t. \quad (\text{C8})$$

Equation C5 then reduces to

$$\frac{\Delta t_L}{t_{\text{col}}} = \frac{1 - \frac{(4-k)\Gamma_1^2}{\Gamma_2^2}}{1 - \frac{1}{2\Gamma_2^2}} \approx 1 - \frac{(4-k)\Gamma_1^2}{\Gamma_2^2}, \quad (\text{C9})$$

where we have ignored the second term in the denominator assuming $\Gamma_2 \gg 1$. For $k = 2$, this gives

$$\Gamma_2 = 2^{1/2} \Gamma_1 \left(1 - \frac{\Delta t_L}{t_{\text{col}}} \right)^{-1/2}. \quad (\text{C10})$$

REFERENCES

- Aloy, M.-A., Ibáñez, J.-M., Miralles, J.-A., & Urpin, V. 2002, *A&A*, 396, 693
- Barthelmy, S. D., Barbier, L. M., Cummings, J. R., et al. 2005, *Space Sci. Rev.*, 120, 143
- Baumgartner, W. H., Barthelmy, S. D., Cummings, J. R., et al. 2014, GRB Coordinates Network, 15927, 1
- Beniamini, P., & Mochkovitch, R. 2017, ArXiv e-prints, arXiv:1705.03900
- Bernardini, M. G., Margutti, R., Chincarini, G., Guidorzi, C., & Mao, J. 2011, *A&A*, 526, A27
- Blandford, R. D., & McKee, C. F. 1976, *Physics of Fluids*, 19, 1130
- Burrows, D. N., Romano, P., Falcone, A., et al. 2005a, *Science*, 309, 1833
- Burrows, D. N., Hill, J. E., Nousek, J. A., et al. 2005b, *Space Sci. Rev.*, 120, 165
- Butler, N., Watson, A. M., Kutyrev, A., et al. 2014a, GRB Coordinates Network, 15937, 1
- . 2014b, GRB Coordinates Network, 15928, 1
- Chevalier, R. A., & Li, Z.-Y. 2000, *ApJ*, 536, 195
- Chincarini, G., Moretti, A., Romano, P., et al. 2007, *ApJ*, 671, 1903
- Chincarini, G., Mao, J., Margutti, R., et al. 2010, *MNRAS*, 406, 2113
- Cordes, J. M., & Lazio, T. J. W. 2002, arXiv:astro-ph/0207156, arXiv:astro-ph/0207156
- Curran, P. A., Starling, R. L. C., O'Brien, P. T., et al. 2008, *A&A*, 487, 533
- Daigne, F., & Mochkovitch, R. 1998, *MNRAS*, 296, 275
- Dall'Oso, S., Perna, R., Tanaka, T. L., & Margutti, R. 2017, *MNRAS*, 464, 4399
- De Pasquale, M., Kuin, N. P. M., Oates, S., et al. 2015, *MNRAS*, 449, 1024
- de Ugarte Postigo, A., Lundgren, A., Martín, S., et al. 2012, *A&A*, 538, A44
- de Ugarte Postigo, A., Gorosabel, J., Xu, D., et al. 2014, GRB Coordinates Network, 15921, 1
- Duffell, P. C., & MacFadyen, A. I. 2015, *ApJ*, 806, 205
- Evans, P. A., Beardmore, A. P., Page, K. L., et al. 2007, *A&A*, 469, 379
- . 2009, *MNRAS*, 397, 1177
- Evans, P. A., Beardmore, A. P., Burrows, D. N., et al. 2014, GRB Coordinates Network, 15915, 1
- Falcone, A. D., Burrows, D. N., Lazzati, D., et al. 2006, *ApJ*, 641, 1010
- Fan, Y. Z., & Wei, D. M. 2005, *MNRAS*, 364, L42
- Fenimore, E. E., Ramirez-Ruiz, E., & Wu, B. 1999, *ApJ*, 518, L73
- Gao, H., Lei, W.-H., Zou, Y.-C., Wu, X.-F., & Zhang, B. 2013, *New Astronomy Reviews*, 57, 141
- Geng, J. J., Wu, X. F., Huang, Y. F., & Yu, Y. B. 2013, *ApJ*, 779, 28
- Ghisellini, G., Nardini, M., Ghirlanda, G., & Celotti, A. 2009, *MNRAS*, 393, 253
- Giannios, D. 2006, *A&A*, 455, L5
- Goodman, J., & Narayan, R. 2006, *ApJ*, 636, 510
- Gorbovskoy, E., Lipunov, V., Pruzhinskaya, M., et al. 2014a, GRB Coordinates Network, 15914, 1
- . 2014b, GRB Coordinates Network, 15932, 1
- Granot, J., Nakar, E., & Piran, T. 2003, *Nature*, 426, 138
- Granot, J., & Sari, R. 2002, *ApJ*, 568, 820
- Greiner, J., Krühler, T., Nardini, M., et al. 2013, *A&A*, 560, A70
- Guidorzi, C., Dichiara, S., Frontera, F., et al. 2015, *ApJ*, 801, 57
- Hascöet, R., Daigne, F., & Mochkovitch, R. 2012, *A&A*, 541, A88
- Holland, S. T., De Pasquale, M., Mao, J., et al. 2012, *ApJ*, 745, 41
- Jenke, P., & Fitzpatrick, G. 2014, GRB Coordinates Network, 15923, 1
- Jeong, S., Sanchez-Ramirez, R., Gorosabel, J., & Castro-Tirado, A. J. 2014, GRB Coordinates Network, 15936, 1
- King, A., O'Brien, P. T., Goad, M. R., et al. 2005, *ApJ*, 630, L113
- Kobayashi, S., Mészáros, P., & Zhang, B. 2004, *ApJ*, 601, L13
- Kobayashi, S., Piran, T., & Sari, R. 1997, *ApJ*, 490, 92
- Kobayashi, S., & Sari, R. 2000, *ApJ*, 542, 819
- Kobayashi, S., & Zhang, B. 2003, *ApJ*, 597, 455
- Kumar, P., Narayan, R., & Johnson, J. L. 2008, *MNRAS*, 388, 1729
- Kumar, P., & Panaitescu, A. 2000, *ApJ*, 541, L51
- Kumar, P., & Piran, T. 2000, *ApJ*, 532, 286
- Lamberts, A., & Daigne, F. 2017, ArXiv e-prints, arXiv:1702.04362
- Laskar, T., Berger, E., Margutti, R., et al. 2015, *ApJ*, 814, 1
- Laskar, T., Berger, E., Zauderer, B. A., et al. 2013, *ApJ*, 776, 119
- Laskar, T., Berger, E., Tanvir, N., et al. 2014, *ApJ*, 781, 1
- Li, L., Liang, E.-W., Tang, Q.-W., et al. 2012, *ApJ*, 758, 27
- López-Cámara, D., Lazzati, D., & Morsony, B. J. 2016, *ApJ*, 826, 180
- Lyutikov, M. 2017, *Physics of Fluids*, 29, 047101
- Mangano, V., Holland, S. T., Malesani, D., et al. 2007, *A&A*, 470, 105
- Margutti, R., Bernardini, G., Barniol Duran, R., et al. 2011a, *MNRAS*, 410, 1064
- Margutti, R., Guidorzi, C., Chincarini, G., et al. 2010a, *MNRAS*, 406, 2149
- Margutti, R., Genet, F., Granot, J., et al. 2010b, *MNRAS*, 402, 46

- Margutti, R., Chincarini, G., Granot, J., et al. 2011b, *MNRAS*, 417, 2144
- Marshall, F. E., & Evans, P. A. 2014, *GRB Coordinates Network*, 15920, 1
- McMullin, J. P., Waters, B., Schiebel, D., Young, W., & Golap, K. 2007, in *Astronomical Society of the Pacific Conference Series*, Vol. 376, *Astronomical Data Analysis Software and Systems XVI*, ed. R. A. Shaw, F. Hill, & D. J. Bell, 127
- Mészáros, P., & Rees, M. J. 1999, *MNRAS*, 306, L39
- Metzger, B. D., Giannios, D., Thompson, T. A., Bucciantini, N., & Quataert, E. 2011, *MNRAS*, 413, 2031
- Morsony, B. J., Lazzati, D., & Begelman, M. C. 2010, *ApJ*, 723, 267
- Nardini, M., Elliott, J., Filgas, R., et al. 2014, *A&A*, 562, A29
- Nousek, J. A., Kouveliotou, C., Grupe, D., et al. 2006, *ApJ*, 642, 389
- Panaitescu, A., Vestrand, W. T., & Wózniać, P. 2013, *MNRAS*, 433, 759
- Perley, D. A., Cenko, S. B., Corsi, A., et al. 2014, *ApJ*, 781, 37
- Perna, R., Armitage, P. J., & Zhang, B. 2006, *ApJ*, 636, L29
- Piran, T. 2005, *Rev. Mod. Phys.*, 76, 1143
- Proga, D., & Zhang, B. 2006, *MNRAS*, 370, L61
- Roming, P. W. A., Kennedy, T. E., Mason, K. O., et al. 2005, *Space Sci. Rev.*, 120, 95
- Rosswog, S. 2007, *MNRAS*, 376, L48
- Sari, R., & Mészáros, P. 2000, *ApJ*, 535, L33
- Sari, R., Piran, T., & Narayan, R. 1998, *ApJ*, 497, L17+
- Sault, R. J., Teuben, P. J., & Wright, M. C. H. 1995, in *Astronomical Society of the Pacific Conference Series*, Vol. 77, *Astronomical Data Analysis Software and Systems IV*, ed. R. A. Shaw, H. E. Payne, & J. J. E. Hayes, 433
- Tagliaferri, G., Goad, M., Chincarini, G., et al. 2005, *Nature*, 436, 985
- Vlasis, A., van Eerten, H. J., Meliani, Z., & Keppens, R. 2011, *MNRAS*, 415, 279
- Volnova, A., Pozanenko, A., Korobtsev, I., Klunko, E., & Eselevich, M. 2014a, *GRB Coordinates Network*, 15917, 1
- Volnova, A., Tungalag, N., Schmalz, S., et al. 2014b, *GRB Coordinates Network*, 15918, 1
- Willingale, R., Genet, F., Granot, J., & O’Brien, P. T. 2010, *MNRAS*, 403, 1296
- Willingale, R., Starling, R. L. C., Beardmore, A. P., Tanvir, N. R., & O’Brien, P. T. 2013, *MNRAS*, 431, 394
- Woosley, S. E., & Bloom, J. S. 2006, *ARA&A*, 44, 507
- Xin, L. P., Pozanenko, A., Kann, D. A., et al. 2012, *MNRAS*, 422, 2044
- Xu, D., Niu, H.-B., Feng, G.-J., et al. 2014, *GRB Coordinates Network*, 15916, 1
- Yu, Y. B., Wu, X. F., Huang, Y. F., et al. 2015, *MNRAS*, 446, 3642
- Zauderer, B. A., Laskar, T., & Berger, E. 2014, *GRB Coordinates Network*, 15931, 1
- Zhang, B., & Mészáros, P. 2002, *ApJ*, 566, 712

ON-LINE ONLY MATERIAL

Table 7
Parameters for best-fit ISM models

Parameter	Model 1	Model 2	Model 3
Ordering at 0.1 d	$\nu_c > \nu_X$	$\nu_c < \nu_{\text{NIR}}$	$\nu_{\text{NIR}} < \nu_c < \nu_X$
p	2.86	2.11	2.73
ϵ_e	2.7×10^{-2}	0.38	3.2×10^{-2}
ϵ_B	1.1×10^{-4}	0.13	2.8×10^{-3}
n_0	1.0×10^{-4}	0.76	4.2×10^{-4}
$E_{K,\text{iso},52}$ (erg)	2.6×10^4	14.1	2.1×10^3
t_{jet} (d)	1.86	1.5	2.5
θ_{jet} (deg)	0.53	3.9	0.98
A_V (mag)	0.08	0.07	0.15
ν_{sa} (Hz)	...	$4.7 \times 10^{8\dagger}$...
ν_{ac} (Hz)	...	1.6×10^{10}	...
ν_a (Hz)	$2.6 \times 10^{7\dagger}$...	$6.6 \times 10^{7\dagger}$
ν_m (Hz)	1.8×10^{14}	8.5×10^{14}	2.8×10^{14}
ν_c (Hz)	1.4×10^{18}	1.0×10^{13}	1.7×10^{17}
$F_{\nu,\text{max}}$ (mJy)	2.1	3.2	1.7
E_γ (erg)			
E_K (erg)	1.1×10^{52}	3×10^{50}	3.1×10^{51}
E_{tot} (erg)			
η_{rad}			

Note. — All break frequencies are listed at 0.1 d. \dagger These break frequencies are not directly constrained by the data.

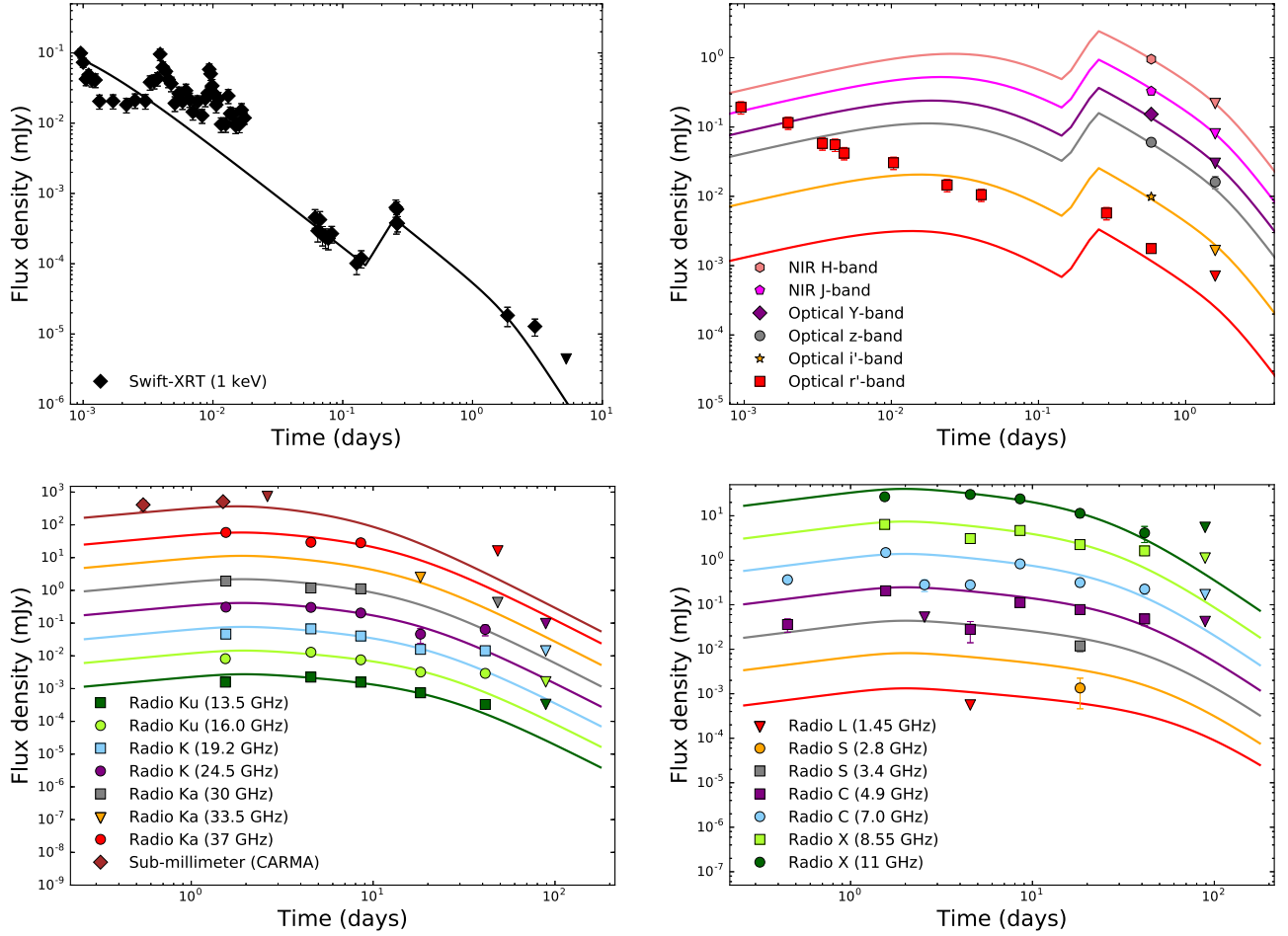


Figure 12. X-ray (top left), optical/NIR (top right) and radio (bottom) light curves of the afterglow of GRB 140304A, together with an FS ISM model with $\nu_{\text{NIR}}, \nu_X < \nu_c$ including energy injection between 0.15 d and 0.26 d (Section 4.3). The model significantly under-predicts the optical light curve before 4×10^{-2} d, and is therefore disfavored.

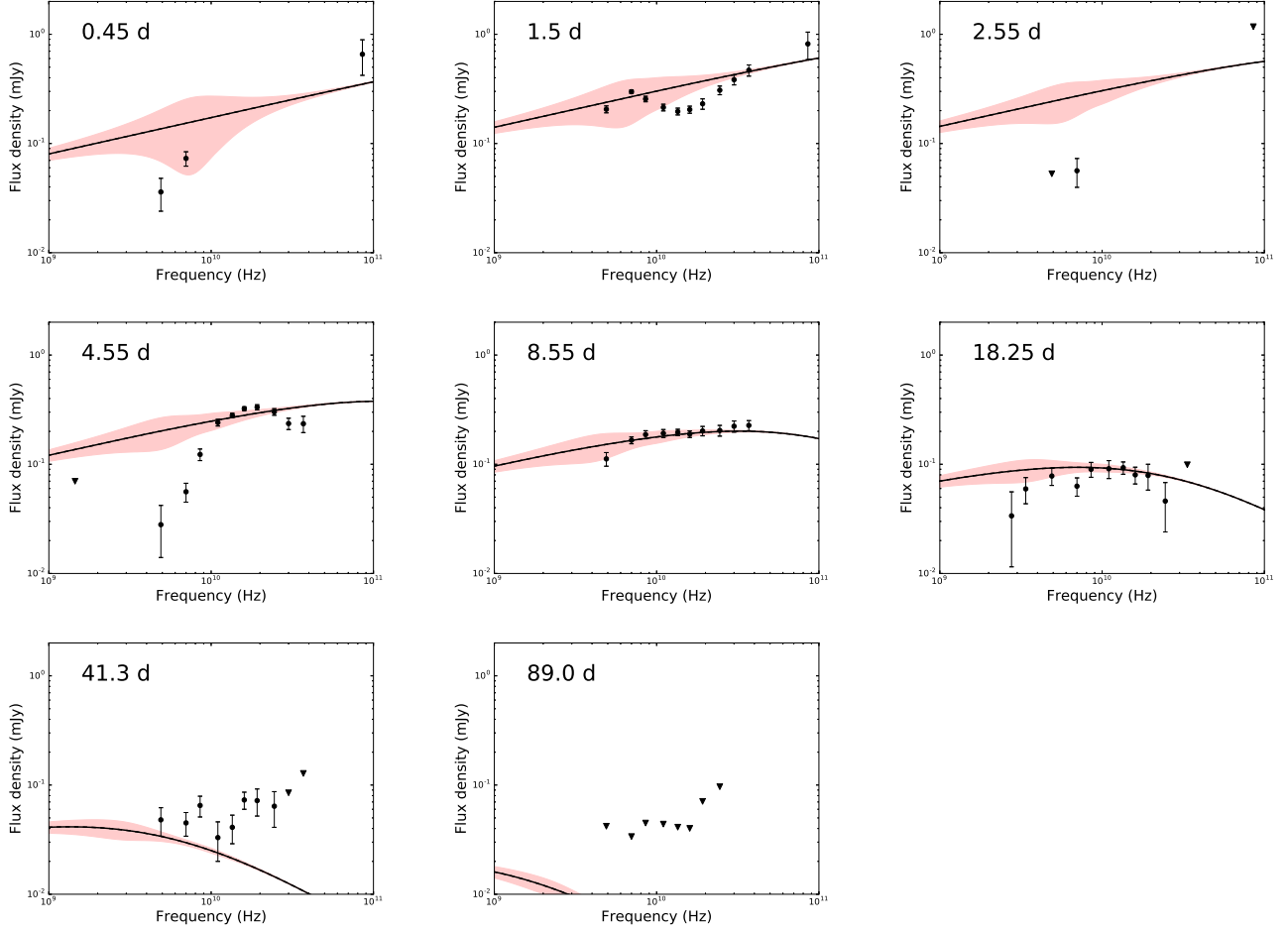


Figure 13. Radio spectral energy distributions of the afterglow of GRB 140304A at multiple epochs starting at 0.45 d, together with the same FS ISM model with $\nu_X < \nu_c$ as in Figure 12. The red shaded regions represent the expected variability due to scintillation.

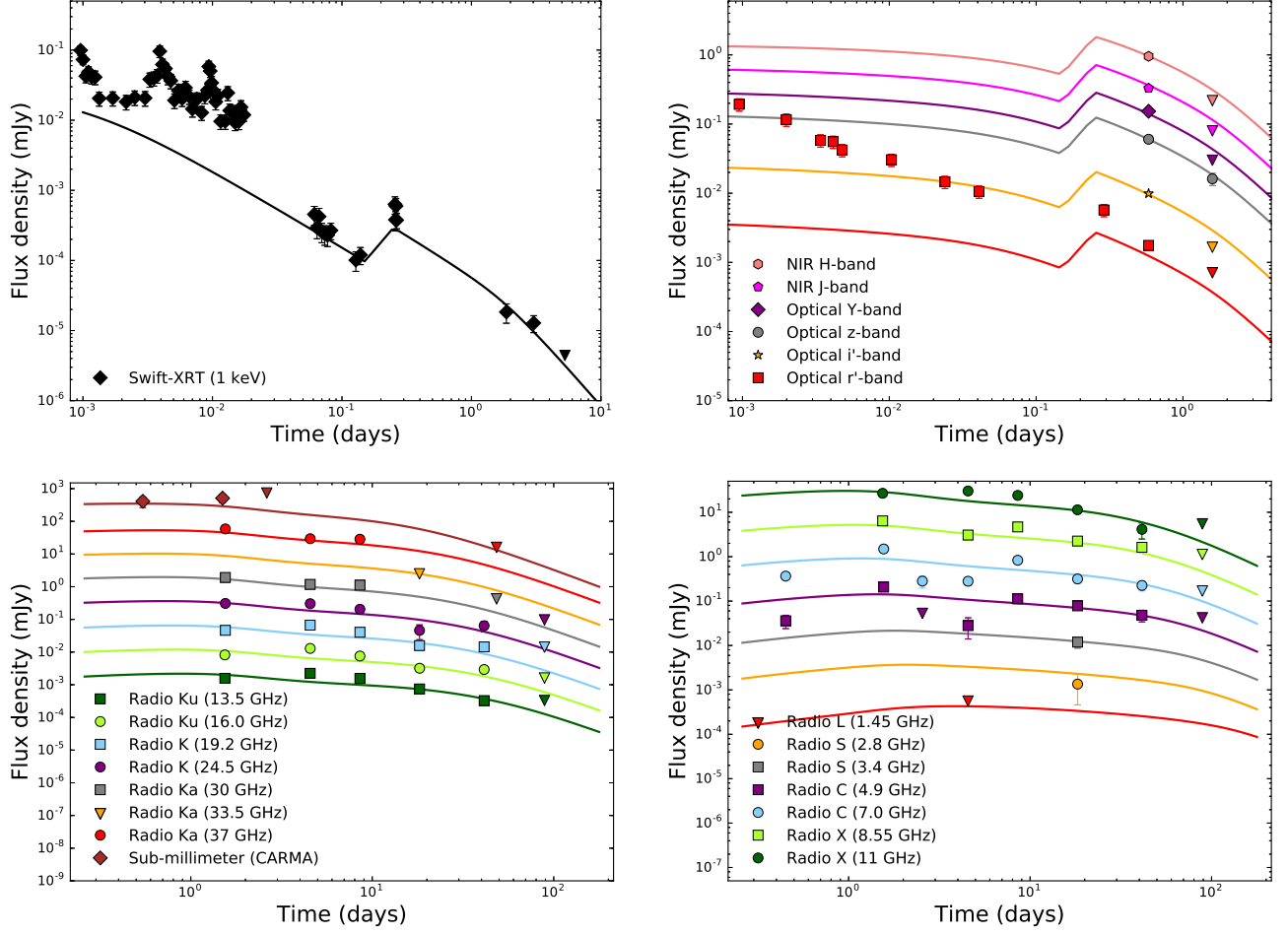


Figure 14. X-ray (top left), optical/NIR (top right) and radio (bottom) light curves of the afterglow of GRB 140304A, together with an FS ISM model with $\nu_c < \nu_{\text{NIR}}$ including energy injection between 0.15 d and 0.26 d (Section 4.3). The model significantly under-predicts the optical light curve before 4×10^{-2} d, and is therefore disfavored.

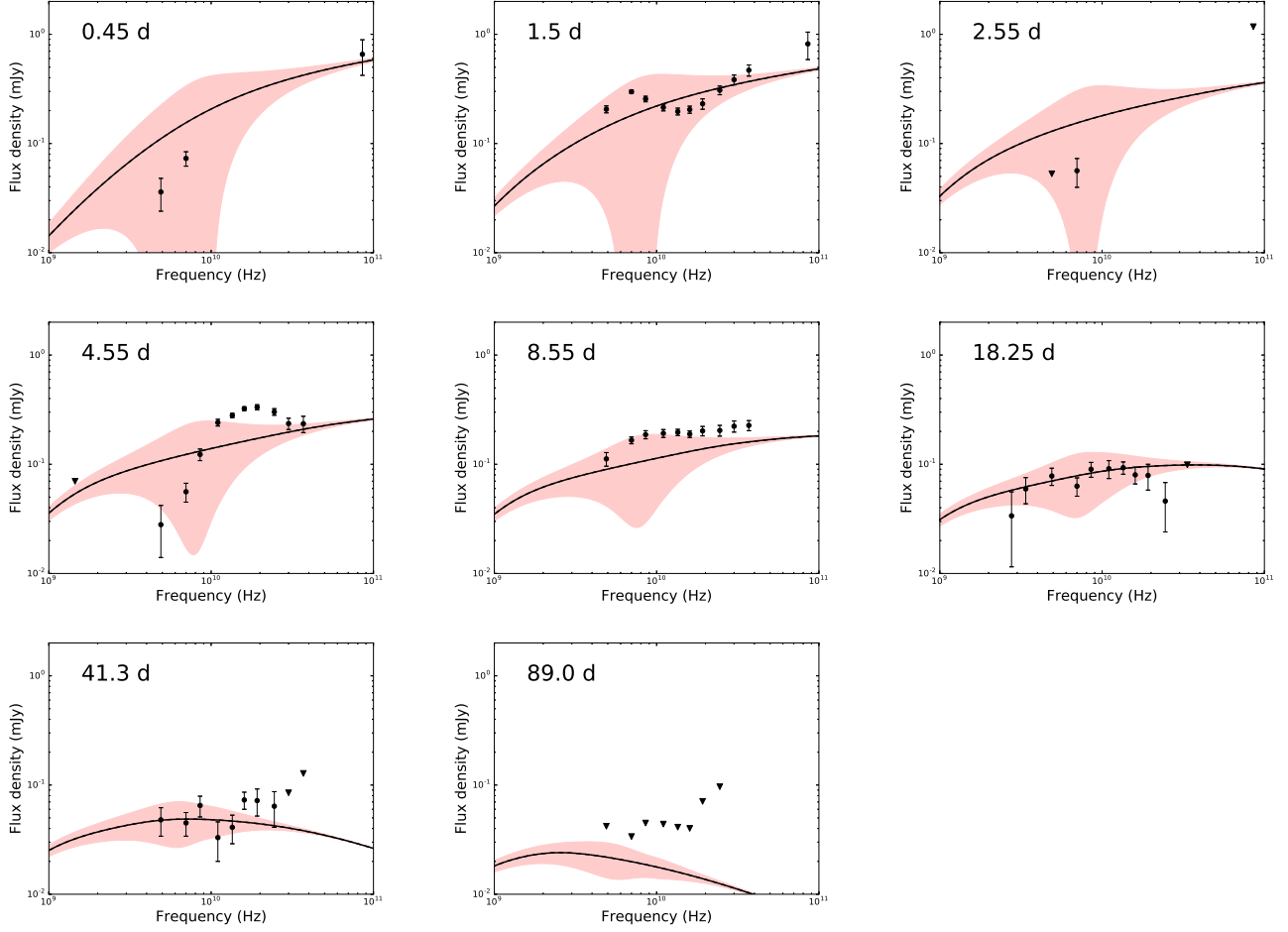


Figure 15. Radio spectral energy distributions of the afterglow of GRB 140304A at multiple epochs starting at 0.45 d, together with the same FS ISM model as in Figure 14. The red shaded regions represent the expected variability due to scintillation.

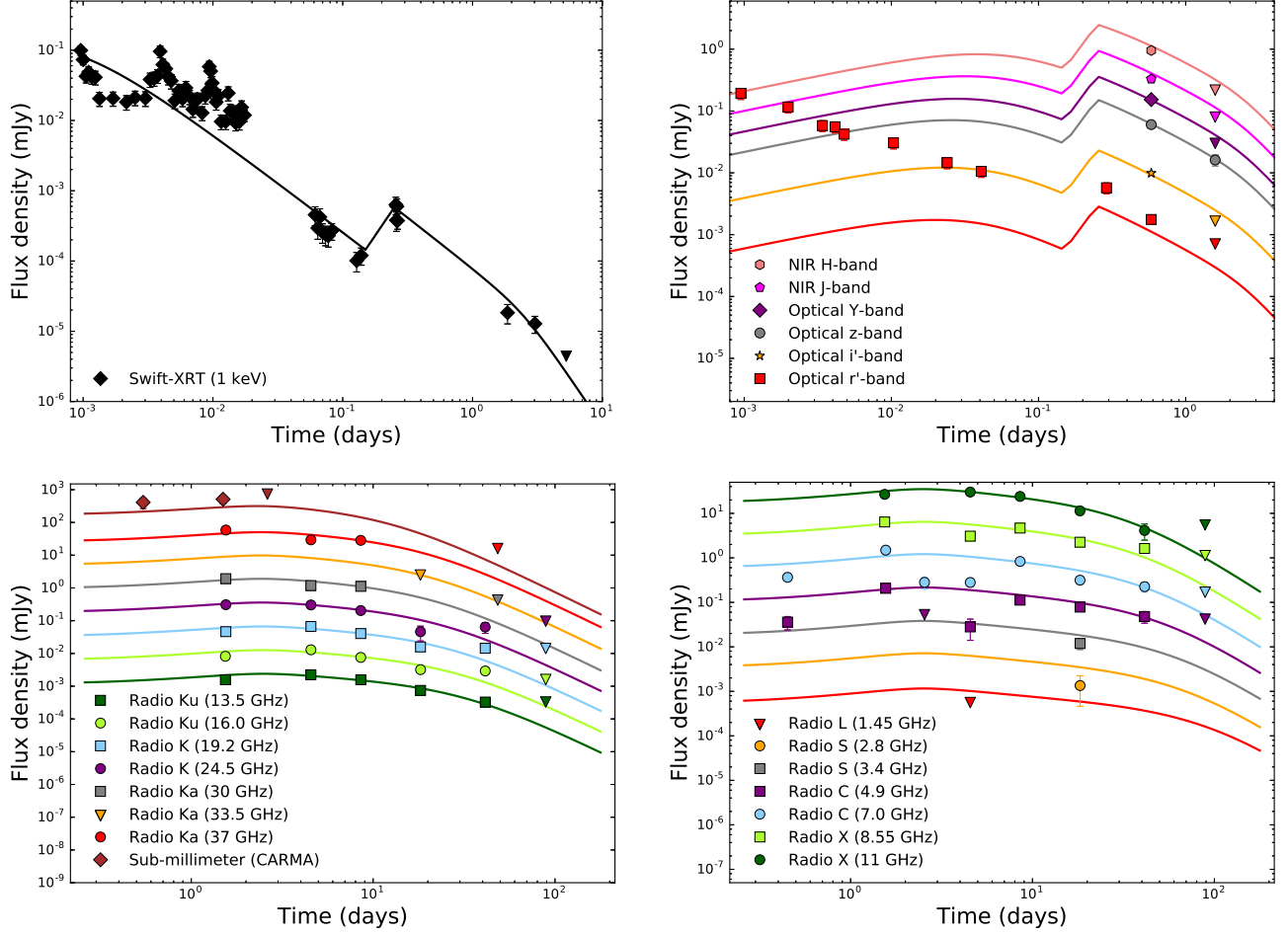


Figure 16. X-ray (top left), optical/NIR (top right) and radio (bottom) light curves of the afterglow of GRB 140304A, together with an FS ISM model with $\nu_{\text{NIR}} < \nu_c < \nu_X$ including energy injection between 0.15 d and 0.26 d (Section 4.3). The different X-ray decay rate expected compared with the case of $\nu_c > \nu_X$ is offset here by a slightly different value of p (Table 7). The model significantly under-predicts the optical light curve before 4×10^{-2} d, and is therefore disfavored.

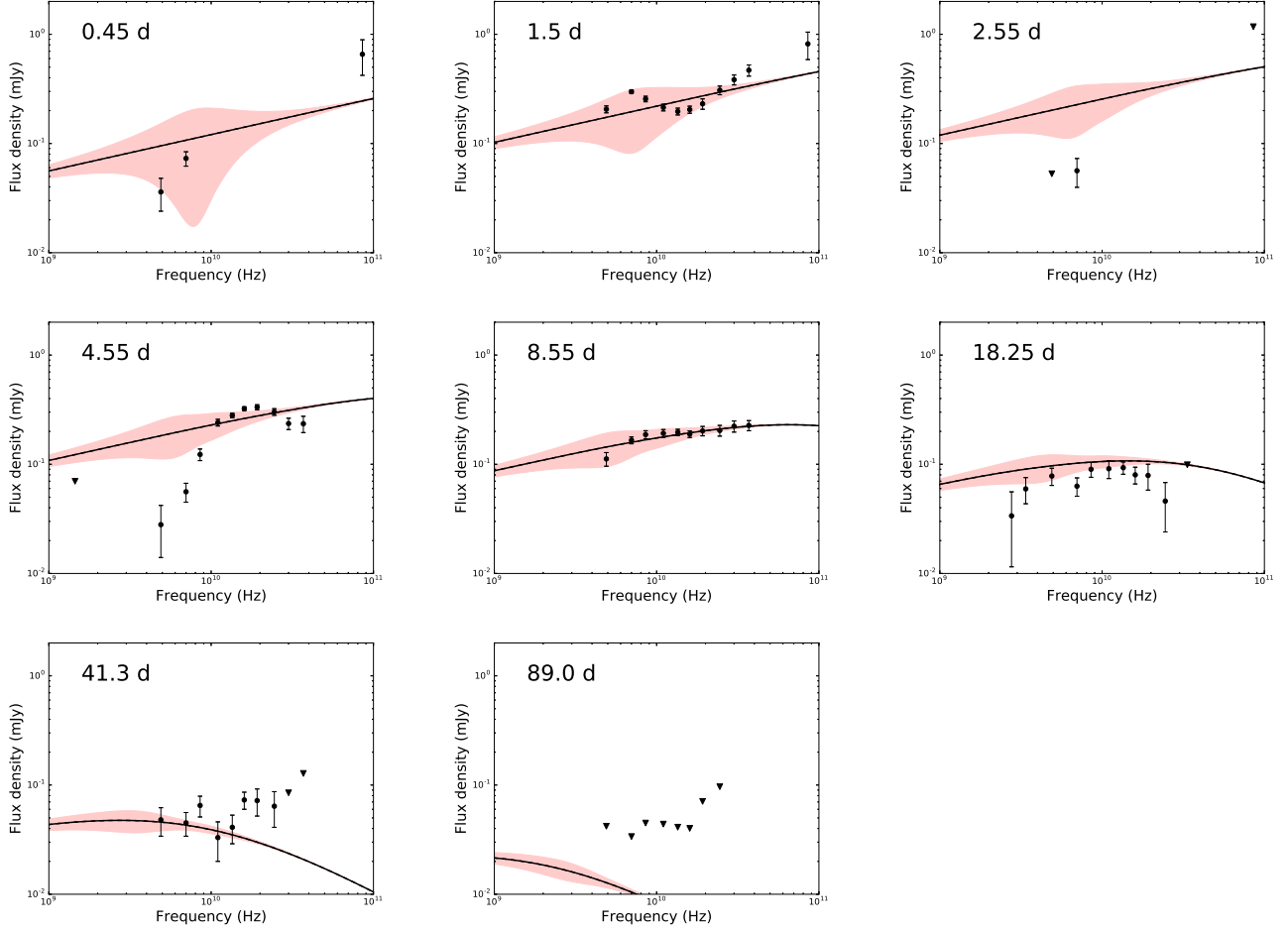


Figure 17. Radio spectral energy distributions of the afterglow of GRB 140304A at multiple epochs starting at 0.45 d, together with the same FS ISM model in Figure 16. The red shaded regions represent the expected variability due to scintillation.